TECHNICAL UNIVERSITY OF CRETE

DIPLOMA THESIS

Optical fibre vibrometers for applications in fragile/sensitive items transportation

---

Author :

Kalligiannakis Konstantinos

Thesis Committee :

Karystinos George

Balas Costas

Pissadakis Stavros

School of Electrical and Computer Engineering - TUC

Institute of Electronic Structure & Laser - FORTH

2025

Acknowledgements

I would like to begin by expressing my sincere gratitude to Mr. Stavros Pissadakis, who, despite being an external collaborating professor, entrusted me, supported me, and guided me throughout the course of this thesis. His experience, dedication to research, and willingness to share his knowledge were crucial to the progress of this work and to my personal academic development. His openness to discussion and his continuous encouragement helped me overcome challenges and deeply engage with the subject of my study.

I would also like to warmly thank Mr. Konstantinos Balas, whose unique lectures – more like creative conversations than traditional classes – served as a true source of inspiration. Especially during the COVID-19 pandemic, he managed to create a vibrant and humane academic environment that helped us escape the hardships of the time and fall in love with Optoelectronics. His approach, far from the rigid nature of standard lectures, encouraged us to participate actively, think critically, and experience science as something living and creative.

A heartfelt thank you also goes to my colleagues at the Foundation for Research and Technology – Hellas (FORTH) —and especially Vasileios Sarakatsianos, who helped me acclimate to the lab environment and supported me with both technical and practical matters. His daily presence, willingness to share knowledge and experiences, and the spirit of teamwork within the lab played a decisive role in making me feel part of a true research community.

I would also like to express my deepest gratitude to my parents, who have been and continue to be the foundation upon which this entire journey was built. They stood by me from the very beginning, offering their unwavering support – emotionally, morally, and practically – enabling me to enter the Technical University of Crete and successfully complete my studies. Without their guidance, advice, and belief in my potential, my academic path would have been far more difficult.

Kalligiannakis Konstantinos

Chania 2025

Abstract

The detection and mitigation of transport-induced damage, particularly in high-value and sensitive objects, remains a critical challenge—especially in the case of micro-damages and micro-vibrations that escape human perception. This work presents a novel optical fiber-based sensor capable of non-invasive vibration monitoring through light intensity modulation. The sensing element of this sensor consists of a single-mode fiber that has been tapered and bent into a U-shape. This configuration increases sensitivity to bending-induced losses, which are detected as variations in transmitted light intensity. This makes the sensor capable of operating without the use of interferometric or grating structures, typically utilized in such applications. The tapered fiber was fabricated using a resistive heating and pulling process, and the final structure was integrated into an experimental setup involving a controlled vibration source. Several input signals were used, including square waves, pseudo-random binary sequences, sinusoids of various frequencies, and audio signals. The sensor output was recorded and analyzed both in the time domain and frequency domain using Fourier Transform methods. All measurements were performed under laboratory conditions, and the results demonstrate that the sensor is capable of responding to variations in mechanical excitation.

Contents

Introduction

Chapter 1

1.1 Optical Fiber Sensors

The demand for miniaturization and enhanced precision in sensing technologies has brought optical fibers to the forefront of interest in the sensing field. Optical fibers are flexible, transparent cylindrical waveguides made of a number of oxide or fluoride glasses, polymers, or biomaterials that guide light over long distances with minimal attenuation and signal dispersion through total internal reflection [1][2]. Optical fiber sensors (OFSs) are sensing devices that utilize optical fibers to detect changes in environmental parameters. OFSs offer advantages over electronic sensors, including immunity to electromagnetic interference, suitability for remote and multi-parameter sensing, and resilience in harsh environments [3]. Their compactness, biocompatibility upon case, and ability to be functionalized make them ideal for biomedical, industrial, and environmental applications [4][5][6].

Several optical configurations —including Fabry–Pérot resonators, Bragg gratings, tapered fibers, and interferometric setups— have led to the application of OFSs in various fields.

OFSs are used in Environmental Monitoring for detecting pollutants in air and water, as well as for monitoring chemical leaks. Tapered fibers and long-period gratings enhance sensitivity to refractive index variations, making them ideal for real-time, remote environmental sensing [7].

In biomedical applications, OFSs are used in vivo monitoring of glucose, pressure, and protein markers. Tapered and functionalized fibers offer enhanced interaction with biological media through fluorescence and evanescent field sensing [8][9].

In the oil and gas industry, OFSs provide accurate downhole measurements —measurements collected within the drilling wellbore— under high-pressure and high-temperature conditions. They also enable distributed monitoring of wells and pipelines [16][17].

1.2 Optical Fiber Sensors in Vibrometry

As it was discussed in the previous section, optical fibers are well-suited for sensing applications due to their structural flexibility, immunity to electromagnetic interference, and adaptability in complex environments. These same operational properties support their implementation in vibration monitoring systems, where different optical mechanisms are used to detect dynamic mechanical displacements with high sensitivity. Optical Fiber Vibrometers are commonly used for structural health monitoring, machine condition monitoring, and vibration analysis in aerospace and civil engineering [10][11][12].

Intensity-modulated sensors operate by measuring changes in light intensity as the fiber experiences deformation due to vibration. These sensors are relatively simple, detecting variations in light transmission when the fiber is bent or stretched [14].

Interferometric sensors based on Fabry-Pérot and Mach-Zehnder configurations utilize the interference of light waves to detect phase shifts induced by mechanical movements. These phase changes occur when vibrations affect the path length of the light traveling through the fiber [15].

Fiber Bragg Grating (FBG) sensors measure strain caused by vibrations by detecting shifts in the wavelength of light reflected by the grating structure. FBGs are particularly useful in scenarios where multiple sensors are needed along a single fiber, allowing for distributed vibration sensing across large structures [13].

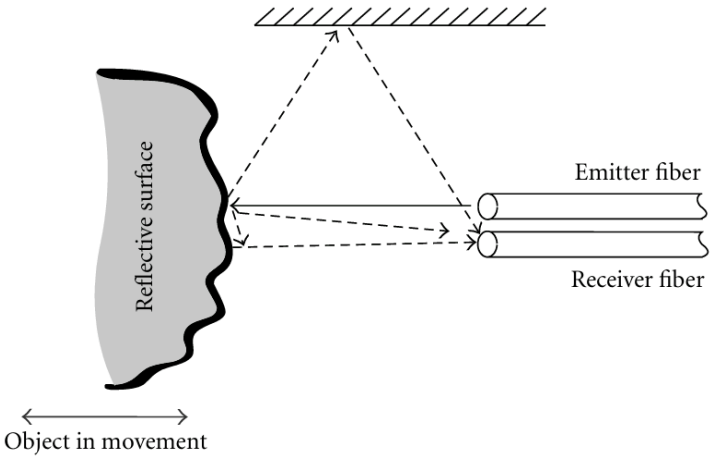

Figure 1.1: Example setup of a dynamic displacement sensor based on intensity variation.

1.3 Optical Fiber Sensing Approach developed in this Thesis

This thesis presents an approach of intensity-based optical fiber vibrometer. A simple sensor configuration is employed, although its fabrication involves certain key techniques.

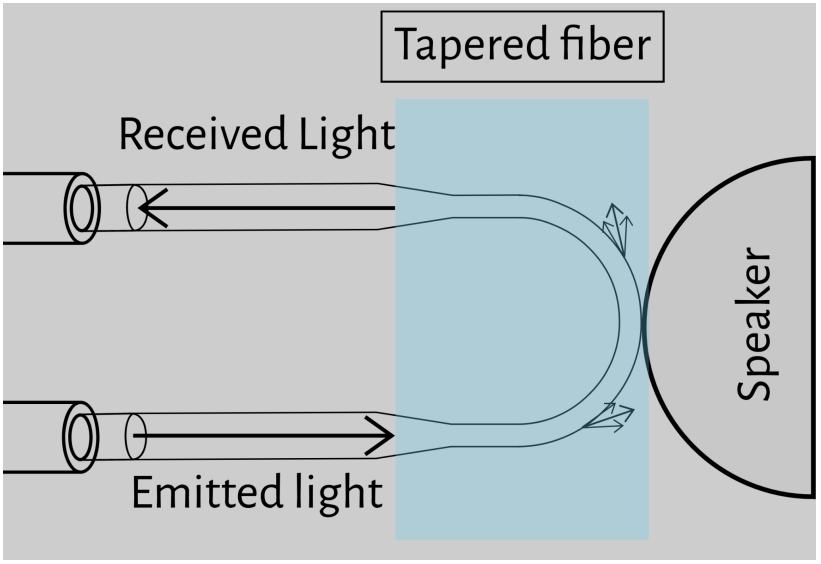

Figure 1.2: Sensor Operation Diagram

The sensor consists of a tapered optical fiber that comes into direct contact with the vibrating object and measures the light transmitted through it. Tapering is a technique in which a high-temperature filament element is used to reduce the diameter of the fiber. As a result, the fiber becomes more sensitive to bending losses, and even minor variations in its curvature significantly affect the intensity of the transmitted light. This approach is suitable for applications where physical contact with the vibrating object is permissible and high measurement accuracy and response speed are required. During the experiments, a loudspeaker is used as the vibrating object, due to the convenience it offers in controlling the vibration signal.

1.4 Thesis Outline

In Chapter 1 the introduction to optical fiber vibrometer sensors was presented. Chapter 2 presents the fundamental theory related to optical fibers, including Maxwell's equations, light guiding conditions, tapered fibers and optical loss mechanisms. Chapter 3 details the experimental implementation of the sensing approach used in this thesis. Chapter 4 discusses the experimental results, focusing on signal behavior and sensor performance. Chapter 5 concludes the thesis with a summary of significant findings and proposals for future work.

Basic theory

Chapter 2

2.1 Maxwell's Equations

To analyze light guiding within an optical fiber, one must first refer to Maxwell's equations and describe, to some extent, their mathematical solution. Maxwell's equations in MKS units are expressed as:

$$\nabla \times E = -\frac{\partial B}{\partial t} \qquad \nabla \times H = J + \frac{\partial D}{\partial t} \qquad \nabla \bullet D = \rho_{free} \qquad \nabla \bullet B = 0$$

For a medium with zero conductivity, these vector relationships may be written in terms of the electric field $\overline{E}$, magnetic field $\overline{H}$, electric flux density $\overline{D}$, and magnetic flux density $\overline{B}$, as the curl equations:

$$\overline{\nabla} \times \overline{E} = -\frac{\partial \overline{B}}{\partial t} \qquad (2.1) \qquad\qquad \nabla \times \overline{H} = \frac{\partial \overline{D}}{\partial t} \qquad (2.2)$$

and the divergence conditions:

$$\overline{\nabla} \bullet \overline{D} = 0 \qquad (2.3) \qquad\qquad \overline{\nabla} \bullet \overline{B} = 0 \qquad (2.4)$$

The four field vectors are related by:

$$\overline{D} = \varepsilon \overline{E} \qquad \overline{B} = \mu \overline{H}$$

Substituting for D and B and taking the curl of eqs. (2.1) and (2.2):

$$\overline{\nabla} \times (\overline{\nabla} \times \overline{E}) = -\mu\varepsilon \frac{\partial^2 \overline{E}}{\partial t^2} \qquad\qquad \overline{\nabla} \times (\overline{\nabla} \times \overline{H}) = -\mu\varepsilon \frac{\partial^2 \overline{H}}{\partial t^2}$$

Then, using the divergence conditions of (2.3) and (2.4) with the vector identity:

$$\nabla \times (\nabla \times Y) = \nabla(\nabla \cdot Y) - \nabla^2 Y$$

we obtain the non dispersive wave equations:

$$\nabla^2 \overline{E} = \mu\varepsilon \frac{\partial^2 E}{\partial t^2} \qquad (2.5) \qquad\qquad \nabla^2 \overline{H} = \mu\varepsilon \frac{\partial^2 H}{\partial t^2} \qquad (2.6)$$

For rectangular and cylindrical coordinates, (2.5) and (2.6) hold for each component satisfying the scalar wave equation:

$$\nabla^2 \psi = \frac{1}{v_p^{\,2}} \frac{\partial^2 \psi}{\partial t^2}$$

where ψ may represent a component of the E or H field, and v_p is the phase velocity (velocity of propagation of a point of constant phase in the wave) in the dielectric medium. It follows that:

$$v_p = \frac{1}{(\mu\varepsilon)^{1/2}} = \frac{1}{(\mu_r \mu_o \varepsilon_r \varepsilon_o)^{1/2}}$$

where μ_r and ε_r are the relative permeability and permittivity.

For the dielectric medium, μ_o and ε_o are the permeability and permittivity of free space. The velocity of light in free space is therefore:

$$c = \frac{1}{\sqrt{\mu_0 \varepsilon_0}}$$

The basic solution of the wave equation is a sinusoidal wave, the most important form of which is a uniform plane wave given by:

$$\psi = \psi_0 e^{i\omega t - \bar{k}\cdot\bar{r}}$$

where ω is the angular frequency of the field and k is the propagation vector, which gives the direction of propagation and the rate of change of phase with distance, whilst the components of r specify the coordinate point at which the field is observed [1][18][19]. When λ is the optical wavelength in vacuum, the magnitude of the propagation vector or the vacuum propagation constant k is given by:

$$k = \frac{2\pi}{\lambda}$$

2.2 Introduction to Optical Fibers

Optical fibers operate based on the optical principle of total internal reflection, which enables the confinement of light within the fiber core. As shown in the Fig (2.1) an optical fiber consists of a central core, typically made of high-purity glass, through which light propagates. Surrounding the core is a cladding layer with a lower refractive index, which ensures that light remains confined within the core by reflecting it internally, usually with similar stoichiometric composition to that of the core. To protect the glass structure from environmental damage and to facilitate handling, a polymer buffer coating is applied over the cladding. This coating aids in the mechanical integrity of the fiber and simplifies processes such as splicing, tapering and termination [1].

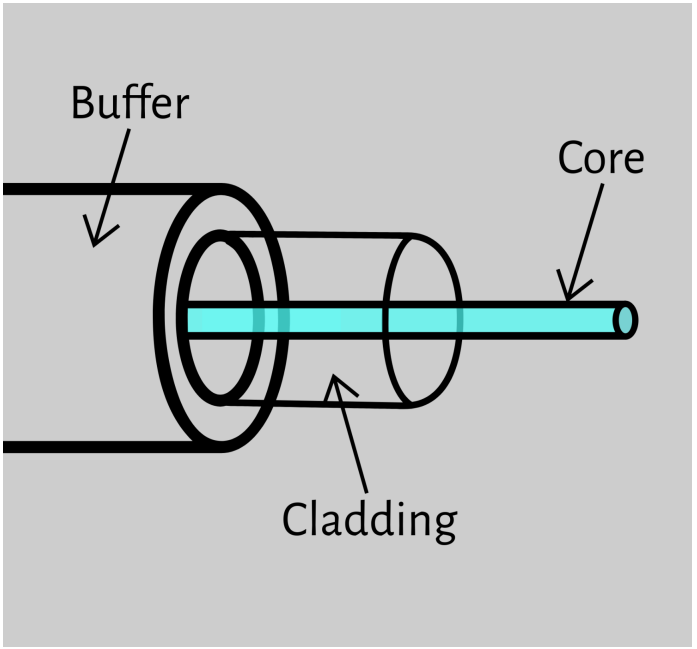

Figure 2.1: Structure of an Optical fiber.

Light propagation within an optical fiber occurs in specific field distributions known as modes. A mode characterizes the spatial distribution of optical power across an electromagnetic-boundary-defined area. The exact mode patterns depend on the wavelength of the transmitted light and the optogeometric parameters of the fiber —core diameter and refractive index contrast between core and cladding.

Fibers capable of supporting multiple modes at a given wavelength are classified as multimode fibers. Accordingly, fibers with suitable core diameter and refractive index contrast can support only a single propagation mode. These are referred to as single-mode fibers, at a specific wavelength. The difference in modal behavior between multimode and single-mode fibers is depicted in the Fig(2.2) [20].

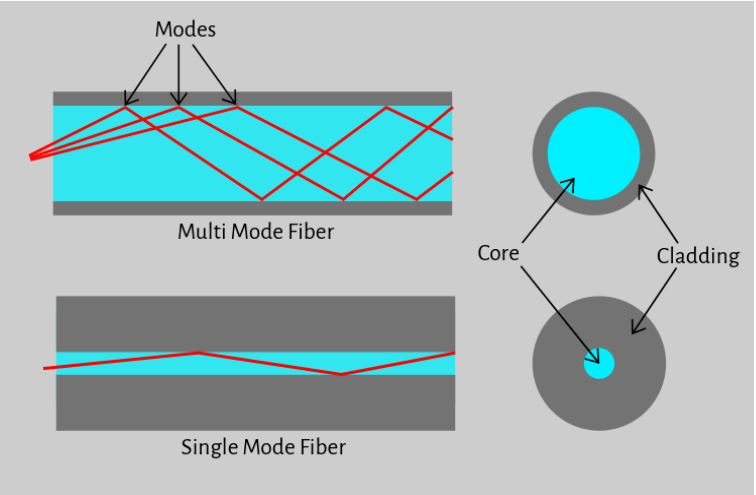

Figure 2.2: Comparison of Single-Mode and Multi-Mode Structural Configurations.

There are two primary types of optical fibers—step-index and graded-index fibers—distinguished by the refractive index profile of their core and cladding regions. In step-index fibers, the core exhibits a uniform refractive index, while the cladding has a lower, also uniform, refractive index —resulting in an abrupt change (or "step") at the core-cladding interface.

In contrast, graded-index fibers feature a refractive index that gradually decreases with increasing radial distance from the fiber axis. This smooth variation enables more efficient mode propagation by continuously refocusing light rays toward the core center, following Fermat principle of shorter propagation time [30]. Graded-index refractive index profiles are typically characterized by specific mathematical functions, such as power-law or parabolic distributions. Fig(2.3) illustrates representative index profiles commonly used in both single-mode and multimode fiber designs [1].

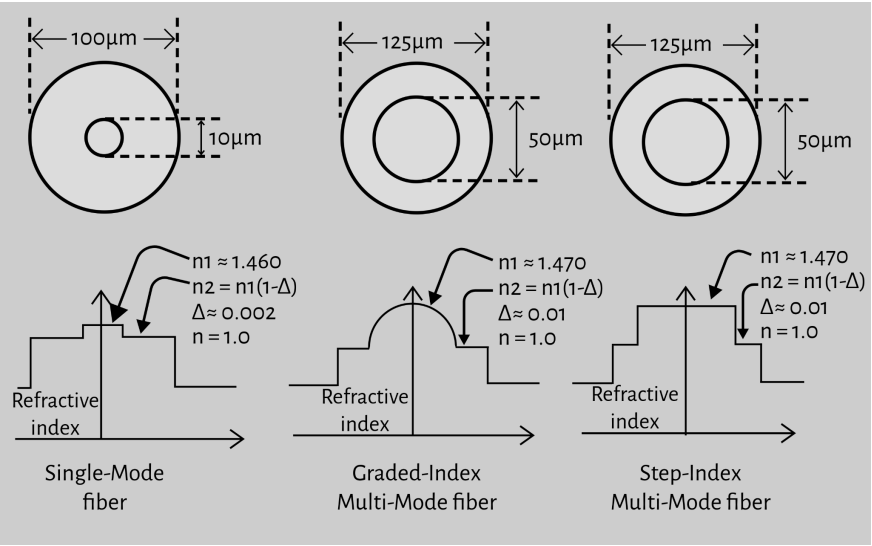

Figure 2.3 :Refractive-index profile for three classes of optical fibers [1].

2.3 Optical Fiber Guiding Conditions

Following the presentation of the fundamental structure and characteristics of optical fibers, attention is now directed toward the analysis of waveguiding conditions in the fiber employed in the sensor, specifically the weakly guiding single-mode fiber.

Consider a cylindrical optical fiber core of radius a. The core exhibits a refractive index n_c, while the surrounding cladding material, assumed to extend to infinity, has a refractive index n. The analysis is conducted using both Cartesian (x, y) and cylindrical (r, φ) coordinate systems.

The propagation constant β of any guided mode supported by this fiber is constrained within the interval $n_c k \geq \beta \geq nk$ (2.7) , where $k = \frac{2\pi}{\lambda}$ denotes the free-space wavenumber.

To proceed, we define the dimensionless parameters:

$$u = a(k^2 n_c^2 - \beta^2)^{\frac{1}{2}} \qquad (2.8)$$

$$w = a(\beta^2 - k^2 n^2)^{\frac{1}{2}} \qquad (2.9)$$

The modal field distribution is represented within the core by the Bessel function $J_l(\frac{ur}{a})$, and in the cladding by the modified Hankel function $K_l(\frac{wr}{a})$. The following identity holds:

$$v^2 = u^2 + w^2$$

which leads to the definition of the normalized frequency parameter:

$$V = ak(n_c^2 - n^2)^{\frac{1}{2}} \qquad (2.10)$$

By enforcing continuity conditions on the field components at the core–cladding interface, one derives characteristic equations in terms of either $u(v)$ or $w(v)$, from which the propagation constant and all secondary modal characteristics can be determined.

In the operating region of weakly guiding, the condition :

$$\Delta = \frac{n_c - n}{n} \ll 1 \qquad (2.11)$$

is satisfied. Under this approximation, the guided modes may be treated as having predominantly transverse electric fields with well-defined polarization states. Although this behavior is established in the literature, a more rigorous derivation is pursued herein through explicit analysis of the transverse field components, (2.12) :

$$E_z = \frac{-iE_1}{2ka} \left\{ \frac{u}{n_{co}} \frac{J_{l+1}(ur/a)}{J_l(u)} sin(l+1)\varphi \right.$$

$$+ \frac{u}{n_{co}} \frac{J_{l-1}(ur/a)}{J_l(u)} sin(l-1)\varphi$$

$$+ \frac{w}{n} \frac{K_{l+1}(wr/a)}{K_l(w)} sin(l+1)\varphi$$

$$\left. - \frac{w}{n} \frac{K_{l-1}(wr/a)}{K_l(w)} sin(l-1)\varphi \right\}$$

$$H_z = \frac{-iE_1}{2ka_0} \left\{ u \frac{J_{l+1}(ur/a)}{K_l(u)} cos(l+1)\varphi \right.$$

$$- u \frac{J_{l-1}(ur/a)}{J_l(u)} cos(l-1)\varphi$$

$$+ w \frac{K_{l+1}(wr/a)}{K_l(w)} cos(l+1)\varphi$$

$$\left. - w \frac{K_{l-1}(wr/a)}{K_l(w)} cos(l-1)\varphi \right\}$$

For core :

$$E_\varphi = \frac{1}{2} E_l \frac{J_{l+1}(ur/a)}{J_l(u)} (cos((l-1)\varphi) + cos((l+1)\varphi))$$

For cladding :

$$E_\varphi = \frac{1}{2} E_l \frac{K_{l+1}(ur/a)}{K_l(w)} (cos((l-1)\varphi) + cos((l+1)\varphi))$$

And for core :

$$H_{\varphi} = -\frac{1}{2}\frac{E_l}{Z_0}\ \frac{n_{c0}J_{l+1}(ur/a)}{J_l(u)}\left(sin((l+1)\varphi) - sin((l-1)\varphi)\right)$$

For cladding :

$$H_{\varphi} = -\frac{1}{2}\frac{E_l}{Z_0}\ \frac{n_{c0}K_{l+1}(wr/a)}{K_l(w)}\left(sin((l+1)\varphi) - sin((l-1)\varphi)\right)$$

The parameter Z_0 corresponds to the intrinsic impedance of free space, while E_l denotes the electric field amplitude at the core-cladding boundary.

Since the relative refractive index difference Δ is considered to be very small, the longitudinal components of the field are negligible compared to the transverse components. Based on this approximation, the modes can be assumed to be linearly polarized (LP).

By setting $n_{co} = n$ in equations (2.12), we obtain the following relation:

$$u\frac{J_{l-1}(u)}{J_l(u)} = -\,w\frac{K_{l-1}(w)}{K_l(w)} \qquad (2.13)$$

This equation represents the characteristic equation for the LP modes. Using the relation $v^2 = u^2 + w^2$ and differentiating equation (2.13) with respect to V, we obtain:

$$\frac{\partial V}{\partial u} = \frac{u}{V}(1 - k_l) \quad (2.14)$$

where

$$\kappa_l = \frac{K_{l^2}(w)}{K_{l-1}(w)K_{l+1}(w)}$$

By applying appropriate approximations, $u(V)$ can be computed from equation (2.14) for all modes.

For higher-order modes, the solution takes the form:

$$u(V) = u_c\frac{e^{arcsin(s/u_c) - arcsin(s/V)}}{s} \qquad (2.15)$$

where u_c is the cutoff value of u and $s = (u_c^2 - l^2 - 1)^{1/2}$.

For the fundamental mode LP_{01}, the expression simplifies to:

$$u(V) = \frac{(1+\sqrt{2})V}{1+(4+V^4)^{1/4}} \qquad (2.16)$$

Using $u(V)$, the propagation constant β can be calculated from equation (2.8).

To generalize the results independently of specific fiber configurations, instead of plotting β directly, we define the normalized propagation constant ratio:

$$b(V) = 1 - \frac{u^2}{V^2} = \frac{(\frac{\beta^2}{k^2}) - n^2}{n_{co}^2 - n^2}$$

which, under the weak guidance approximation, simplifies to:

$$b(V) \approx \frac{\beta/k - n}{n_{co} - n}$$

From equations (2.11) and (2.18), the propagation constant β can be expressed as:

$$\beta = nk[1 + \Delta - \Delta(\frac{u^2}{V^2})]$$

Plotting the normalized parameter $b(V)$ provides valuable insights into the behavior of single-mode fibers (SMFs).

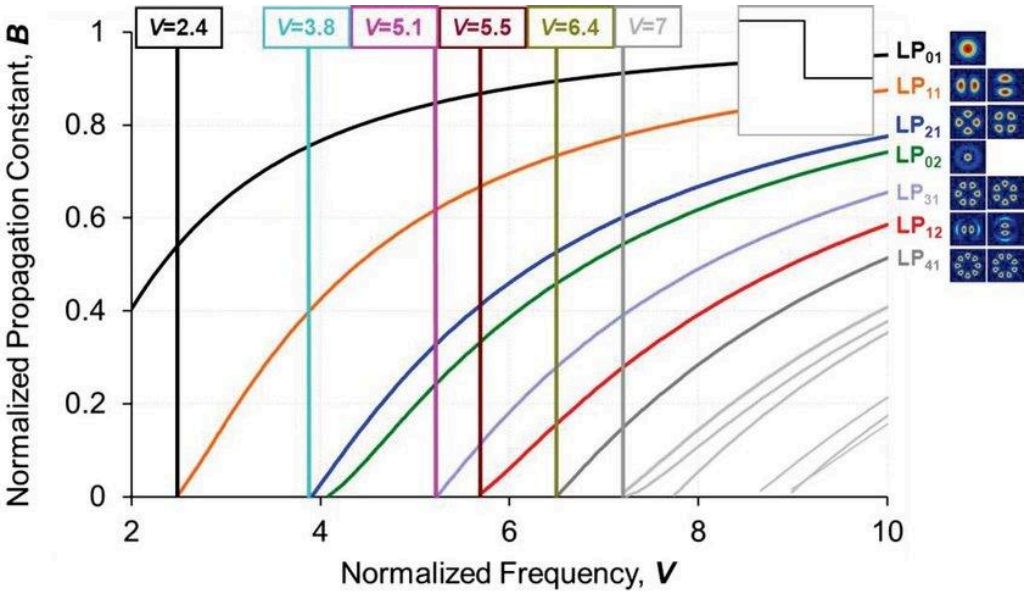

Figure 2.4: Normalized propagation parameter $b(V) \approx \frac{\beta/k - n}{n_{co} - n}$ as a function of the normalized frequency V [21].

From Fig(2.4), it can be concluded that there exists a specific range of normalized frequency values V within which only the LP_{01} mode is supported. This range lies between 0 and approximately 2.405. This threshold serves as a fundamental design criterion for optical fiber engineers, establishing the permissible values of the core radius a, core refractive index n_{c0}, and cladding refractive index n for an optical fiber to operate as a single-mode fiber (SMF) [22]. Therefore, for a given numerical aperture, the core diameter must fall within a precise interval to ensure single-mode propagation.

2.4 Optical Fiber Tapers

A tapered fiber is created by stretching a heated conventional single-mode fiber (SMF), resulting in a structure with a gradually decreasing core diameter. As illustrated in Fig(2.5), the narrowest section of the tapered fiber is referred to as the waist. Between the uniform, unstretched SMF and the waist are the transition regions, where both the cladding and core diameters taper from their original dimensions down to the micrometer or even nanometer scale [23].

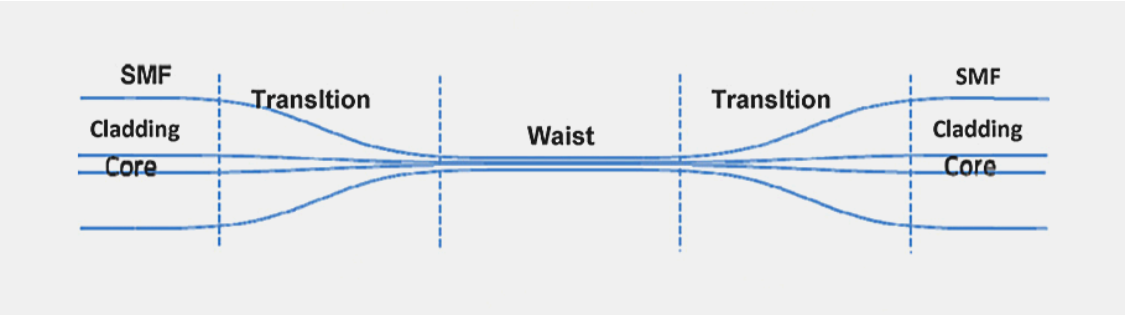

Figure 2.5 :Typical diameter profile of a tapered fiber.

As light propagates through these transition regions, the field distribution evolves in response to the changing core and cladding diameters. Depending on the rate at which these diameters change, energy from the fundamental mode may couple into a few of the nearest higher-order modes, affecting the wave's transmission efficiency. The cumulative effect of such mode coupling throughout the taper can lead to significant transmission loss [24][25].

This excessive loss can be minimized if the shape of the tapered fiber adheres to the adiabaticity condition throughout its two transition lengths. Fig(2.6) illustrates a tapered fiber with a progressively decreasing radius, where z represents the position along the taper.

Theoretically, for a fiber to be adiabatic, the beat length between the fundamental LP_{01} mode and the second local mode must be smaller than the local taper length scale z_t.

$$z_b < z_t$$

As shown in below, z_t is given by

$$z_t = \frac{\rho}{tan\Omega}$$

where $\rho = \rho(z)$ is the local core radius and $\Omega = \Omega(z)$ is the local taper angle. The beat length between two modes is expressed as

$$z_b = \frac{2\pi}{\beta_1 - \beta_2}$$

where $\beta_1 = \beta_1(r)$ and $\beta_2 = \beta_2(r)$ are the propagation constants of fundamental mode and second local mode respectively. From the above equations, Inequality of the tapered fiber can be derived to :

$$\left|\frac{d\rho}{dz}\right| = tan\Omega < \frac{\rho(\beta_1 - \beta_2)}{2\pi}$$

where $\frac{d\rho}{dz}$ is the rate of change of local core radius and its magnitude is equivalent to $tan\Omega$.

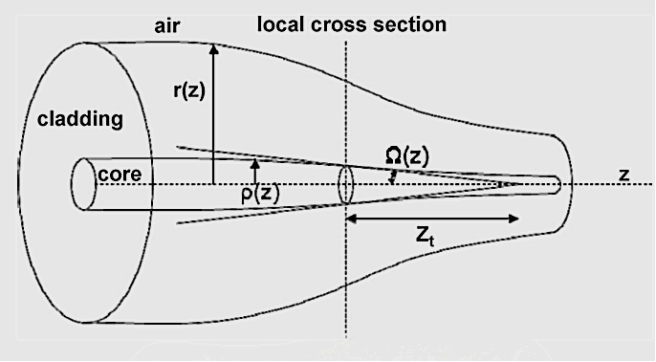

Figure 2.6 :Illustration of the taper transition.

For the convenience of usage and analysis, the inequality of the above equation can also be rewritten as a function of local cladding radius $r = r(z)$ as :

$$\left|\frac{dr}{dz}\right| < \frac{r(\beta_1 - \beta_2)}{2\pi}$$

Based on this condition, an adiabatic tapered fiber can be acquired by reducing the fiber diameter at a slower rate. However, this results in a longer transition region. Due to practical constraints in fabricating fiber couplers or microfiber-based devices, excessively long tapered fibers can make the fabrication process more challenging. For miniaturization purposes, a shorter tapered fiber is more desirable.

To strike a balance between taper length and diameter reduction rate, a factor f is introduced into the inequality function, leading to the condition :

$$\left|\frac{dr}{dz}\right| < \frac{fr(\beta_1-\beta_2)}{2\pi}$$

where f is a coefficient ranging from 0 to 1. The optimal taper profile is achieved when $f = 1$. In practice, tapered fibers with negligible loss can be fabricated with $f = 0.5$, though the resulting taper length will be approximately twice that of the optimal profile.

When a glass element is heated, its volume slightly increases due to thermal expansion. However, this change is minimal and typically disappears rapidly once the heat source is removed. Thus, it is reasonable to assume that the total volume of the heated fiber remains constant throughout the tapering process.

Based on this principle, stretching a heated glass fiber leads to a decrease in waist diameter. The relationship between the changing waist diameter and elongation length can be derived from the concept of volume conservation. Birks and Li proposed simple mathematical expressions to describe how the shape of a tapered fiber relates to elongation distance and the length of the hot zone [24]. By precisely controlling these parameters during the tapering process, specific fiber shapes can be achieved [25].

Fig(2.7) provides schematic illustrations of a heated fiber undergoing diameter reduction during the elongation process.

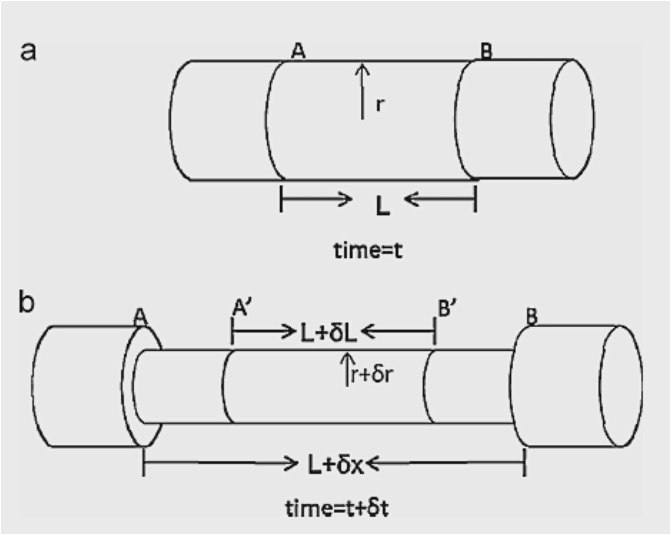

Figure 2.7 : The cylinder illustrates an SMF (a) before heating (b) a short while after heating, where the diameter of the SMF has been reduced when it is stretched.

At time t , the section of heated fiber between cross-sections A and B has a length equal to the hot-zone length L, and its waist diameter is denoted by r. After a short time interval δt the fiber is stretched, increasing its length to $L + \delta x$, while the waist diameter changes to $r + \delta t$, where δr represents the change in radius. Assuming volume conservation during the tapering process, the volume of the fiber at time $t + \delta t$ should be equal to the volume at time t :

$$\pi(r + \delta r)^2(L + \delta x) = \pi r^2 L$$

By performing some algebraic simplifications and taking the limit as the interval approaches zero, a differential equation can be derived to:

$$\frac{dr}{dx} = \frac{r}{2L}$$

The solution to this differential equation provides the profile of the fiber radius along the taper:

$$r(x) = r_0 exp(-\frac{1}{2}\int \frac{dx}{L})$$

where r_0 is the initial radius of the fiber. To relate the hot-zone length L to the elongation distance x during the tapering process, L can be expressed as a function of x. A simple and practical choice is a linear function:

$$L(x) = L_0 + \alpha x$$

Substituting this into the previous equation yields:

$$r(x) = r_0 exp(-\frac{1}{2}\int \frac{dx}{L_0+\alpha x})$$

Solving the integral results in:

$$r(x) = r_0(1 + \frac{ax}{L_0})^{-1/2\alpha}$$

To link the elongation distance *x* with the axial position z along the tapered region, we refer to the model shown in Fig(2.8).

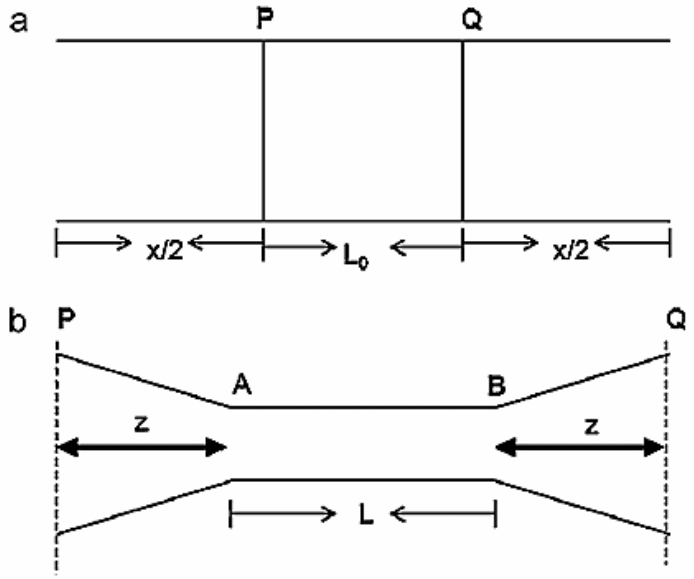

Figure 2.8: Shape of a fiber (a) at the beginning (t = 0) (b) after tapering (time = t).

In Fig(2.8) , L_0 denotes the initial hot-zone length between cross-sections P and Q, while x represents the total elongation distance [25].

Assume the heated fiber is symmetrically stretched to form a biconical taper, resulting in two identical taper sections extending from both ends of the hot zone, each of length $x/2$. After tapering for time t, the points P and Q have moved outward by a total distance of x , and the taper waist has a length P.

From this geometric description, the following relationship can be established:

$$2z + L = x + L_0$$

where $L = L(x)$. Now, the radius as a function of axial position z becomes:

$$r(z) = r_0(1 + \frac{2az}{(1-a)L_0})^{-1/2\alpha}$$

where α is a shaping parameter that can take values between −1 and 1.

By adjusting the value of α, different taper profiles can be achieved —such as reciprocal curves, decaying exponential shapes, linear tapers, and concave geometries. Several examples of taper profiles computed for different values of α can be found.

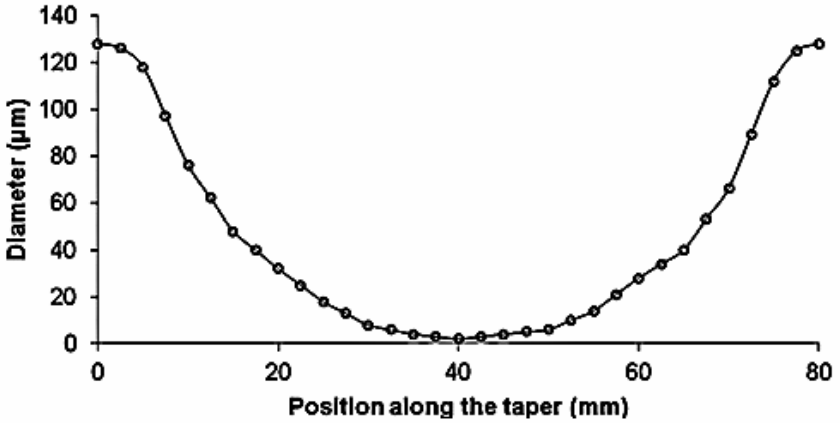

Figure 2.9: A tapered fiber with decaying-exponential profile fabricated using a constant hot-zone L_0 = 10 mm.

Fig(2.9) illustrates the profile of a tapered fiber fabricated using a constant hot-zone length, L_0 = 10 mm. As shown in the figure, the resulting taper has a decaying exponential profile, which corresponds to a fabrication process with a constant hot-zone length (α = 0).

According to the theoretical model described above, the equation that defines this decaying-exponential taper shape is:

$$r(z) = r_0 e^{-z/L_0}$$

This profile is commonly used due to its smooth transition and compatibility with adiabatic conditions, minimizing transmission loss during light propagation through the taper [25].

2.5 Loss Mechanisms in Optical Fibers

Transmission losses in single-mode optical fibers primarily arise from three mechanisms: intrinsic material absorption, scattering (predominantly Rayleigh scattering), and bending-induced radiation losses. Among these, bending loss is particularly significant in determining the optimal design parameters of the fiber. Bending-related losses are typically categorized into two types: (1) radiation losses resulting from uniform bending, and (2) losses associated with random variations in the fiber's curvature.

The bending loss per unit length in step-index single-mode fibers is given by the following expression [26]:

$$\alpha = \frac{1}{2}\left(\frac{\pi}{\alpha W^3}\right)^{1/2}\left(\frac{U}{VK_1(W)}\right)^2 exp(-D \cdot R) \cdot R^{-1/2}$$

$$D = \frac{4\Delta W^3}{3aV^2}$$

where a, R and are the core radius, bending radius, and core-cladding refractive index difference, respectively. K_1 is a modified Hankel function, U and W transverse propagation constants in the core and cladding, respectively, and V is the normalized frequency.
As can be seen from the equations above, the core diameter plays a crucial role in the losses. Fig(2.10) illustrates the calculated bending loss for a step-index single-mode fiber at 1550 nm. The refractive indices of the cladding and core were assumed to be 1.444 and 1.449, respectively. Bending loss increases sharply as the bending radius decreases, and it is highly sensitive to the core size when all other parameters are held constant [29].

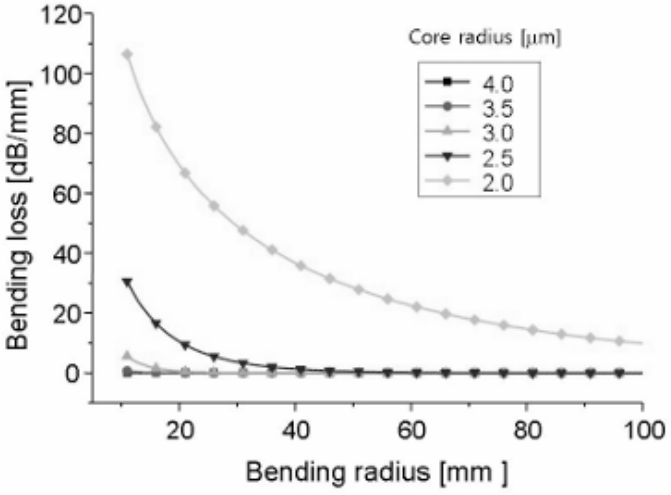

Figure 2.10: The bending radius dependence of the bending loss and the effect of the core size on the bending loss.

A tapered single-mode fiber behaves similarly to a multimode fiber when the refractive index of the external medium surrounding the tapered section is lower than that of the fiber cladding. Mode coupling between the core mode and cladding modes takes place as the tapered fiber bends, causing the bending loss to oscillate with variations in bending curvature [27][28]. During the tapering process, as the diameters of both the core and cladding reduce, the cladding effectively assumes the role of the core, while the low-index external medium acts as the cladding. This allows higher-order modes to propagate within the tapered region, resulting in oscillatory bending loss behavior as the bending radius changes [29].

In the simulation of the Fig(2.11) the beam propagation method was employed to evaluate the transmission loss and bending effects in tapered fibers. The refractive indices of the core and cladding were set to 1.449 and 1.444, respectively. Fig(2.11) presents the calculated mode propagation and excess loss of tapered fibers without bending. For a tapered fiber with diameter reduced to 4.0 μm, the optical beam propagates with negligible loss, as illustrated in Fig. 2.11(a). However, when the diameter decreases further to 3.0 μm, the loss becomes substantial, as shown in Fig. 2.11(b).

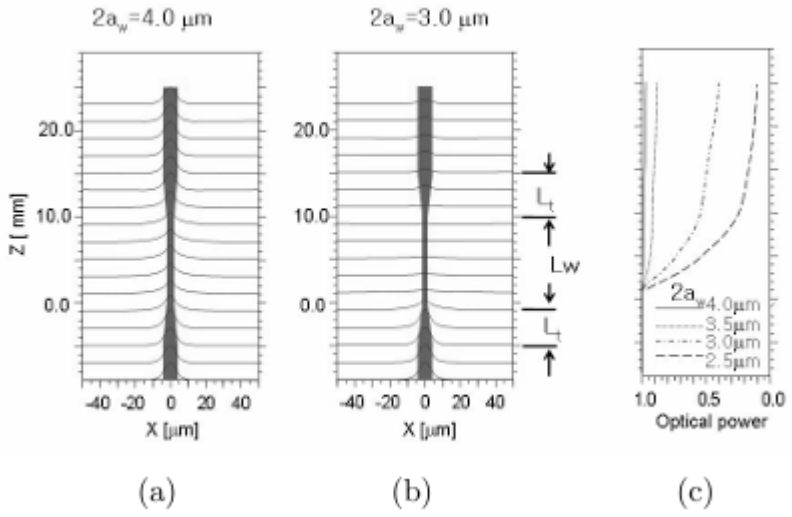

Figure 2.11: Simulation results of a tapered fiber without bending; (a) mode propagation of tapered fiber with 2.0 m core radius at the waist, (b) mode propagation of μ μ tapered fiber with 1.5 m core radius at the waist, (c) optical power variation along the tapered fiber under four different tapering conditions.

This transmission loss mainly arises due to the insufficient length of the tapered fiber section to enable adiabatic mode conversion. Smaller core diameters require longer transition lengths to maintain low transmission loss. For instance, a tapered single-mode fiber with a 3 μm core diameter requires a transition length of about 20 mm to achieve over 90% transmission

efficiency. Fig. 2.11(c) illustrates the reduction of optical power along tapered fibers with different core sizes. Practically, there is a limit to how much the core diameter of a tapered fiber for an OFS can be reduced, since excessive transmission loss may occur along with the expanded mode profile, causing beam power to leak into the external medium [29].

Fig(2.12) displays mode propagation and bending loss in bent fibers, both tapered and untapered. In Fig. 2.12(a), the optical mode passes through the bent region of a uniform core fiber with minimal loss. Conversely, Fig. 2.12(b) shows that bending loss is considerably higher in the bent section of a tapered fiber. Figure 2.12(c) presents the calculated optical power along tapered fibers with four different core diameters at the waist. The tapering ratio (a_0/a_w) must be carefully chosen to balance low excess loss with sufficient bending loss. Based on the results in Figures (2.11) and (2.12), the optimal tapering ratio is around 2.0 for a standard single-mode fiber.

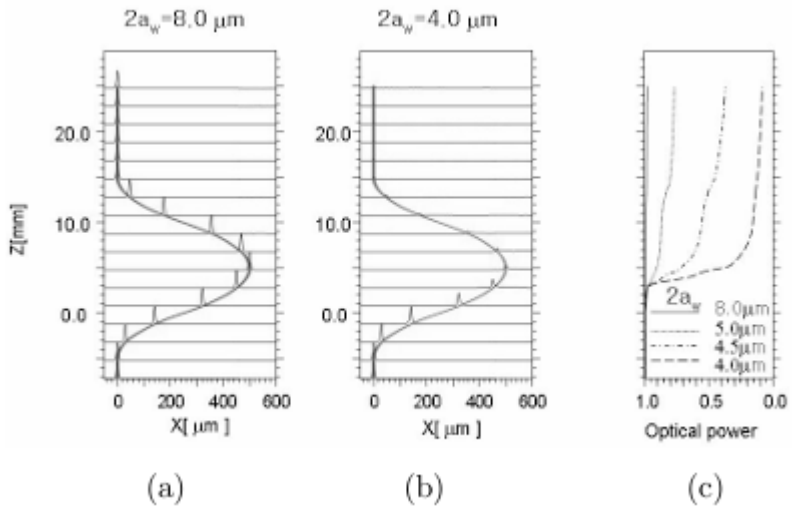

Figure 2.12 :Simulation results of tapered fiber with bending; (a) mode propagation of non tapered fiber, (b) mode propagation of tapered fiber with 2.0 m core radius at μ the waist, (c) optical power variation along the tapered fiber for four different tapering conditions.

In these simulations, the cladding diameter was assumed to be infinite. However, in real devices, the cladding diameter is finite, and the bending loss is influenced by the refractive index of the external medium covering the tapered region —this is an observation for the future work [29].

Experimental

Chapter 3

3.1 Experimental apparatus

3.1.1 Properties of SMF-28 optical fiber

For the development of our sensor, SMF-28™ optical fiber was exclusively used as its main platform. SMF-28™ is a step-index single-mode fiber (SMF) developed by Corning®. Specifically, this optical fiber consists of a fused silica cladding surrounding a GeO_2-doped silica core. The GeO_2doping raises the refractive index of the core, enabling efficient light guiding. Additionally, the presence of GeO_2enhances the fiber's overall optical performance, which is critical in intensity-based sensing applications such as the vibrometer described in this work.

Properties of SMF-28™	
Core Diameter	8.2 µm
Cladding Diameter	~125 µm
Refractive Index Difference	0.36%
Effective Group Index of Refraction	1.4682 at 1550 nm
Mode-field Diameter	10.4 ±0.8 µm at 1550 nm
Cutoff Wavelength (λ_{cf})	$\lambda_{cf} \leq$ 1260 nm
GeO_2-Core Doping Levels	~3.6 mol %

Figure 3.1 : Physical and optical properties of SMF-28™ [31]

3.1.2 Yokogawa Ando AQ8201-13 Light Source Module

Figure 3.2 : Photography of Yokogawa Ando with a AQ8201-13 module.

In the experiment, the light source used was the Yokogawa Ando AQ8201-13. This module is an External Cavity Laser (ECL) module designed for integration into the AQ8200 series optical test systems. It provides a tunable laser source with a wavelength range spanning from 1460 nm to 1580 nm, suitable for applications in optical component testing and fiber optic communication systems. The module offers a wavelength setting resolution of 10 pm and an accuracy of ±0.2 nm, facilitating precise wavelength selection. Optical output is delivered through an FC/APC connector, with measured output power reaching up to +10.3 dBm. These characteristics make the AQ8201-13 suitable for tasks requiring stable and narrow-linewidth light sources, such as the optical sensor under test in this experiment [32].

AQ8201-13 ECL Module (Light Source)	
Available wavelength range	1460 – 1580 nm
Wavelength setting range	10 pm
Wavelength accuracy	±0.2 nm
Wavelength repeatability	±50 pm
Spectral width	100 MHz (Coherence ON)
Optical output level	+10 dBm (typ.)
Output level stability	±0.005 dB (15 min)
SMSR	≥ 45 dB
Optical connector	FC/APC
Applicable fiber	SM (10/125 μm)

Figure 3.3 : Specification table of AQ8201-13 [32]

3.1.3 DET01CFC Photodetector

Figure 3.4 : Photography of DET01CFC Photodetector.

To measure the optical power transmitted through the sensor, a junction photodiode — DET01CFC by Thorlabs — was used. A junction photodiode is an intrinsic semiconductor device that generates photocurrent when light is absorbed in its depletion region. Functionally similar to a signal diode, it operates as a fast, linear detector with high quantum efficiency. Accurate determination of the output current and responsivity depends on the incident optical power.

The total output current of the photodetector can be described by the equation:

$$I_{out} = I_{dark} + I_{PD}$$

where I_{dark} is the dark current and I_{PD} is the photocurrent generated by the incident light.

DET01CFC is a ready-to-use, high-speed InGaAs photodetector designed for operation in near-infrared (NIR) optical systems with FC/PC connectorized fiber optic cables. It includes an FC/PC bulkhead connector, a photodiode, and a 12 V bias battery housed in a compact aluminum enclosure. The FC/PC interface allows efficient coupling to fiber-based light sources, while the output is provided via an SMA jack to minimize physical dimensions and support high-frequency response. The detector operates over a spectral range of 800–1700 nm with a maximum bandwidth of 1.2 GHz [33].

DET01CFC		
Parameter	Symbol	Value
Detector	–	InGaAs PIN
Active Area Diameter	–	Ø0.12 mm
Wavelength Range	λ	800 to 1700 nm
Peak Wavelength	λ_p	1550 nm
Peak Response	$\Re(\lambda_p)$	0.95 A/W (Typ.)
Bandwidth (-3 dB)	–	1.2 GHz
Saturation Power (CW)	–	5.5 mW (1550 nm)
Damage Threshold	–	18 mW
Bias Voltage	V_r	12 V
Dark Current	I_D	0.235 nA
Output Voltage	V_{out}	0 to 1 V (50 Ω) / 0 to 10 V (Hi-Z)
Input	–	FC/PC Fiber Connector
Output	–	SMA (DC Coupled)

Figure 3.5 : Specification table of DET01CFC [33].

3.1.4 PicoScope 4424A Oscilloscope

Figure 3.6 : Photography of PicoScope 4424A.

To acquire the photodetector measurements and analyze the signals, the PicoScope 4424A oscilloscope was used. It is a four-channel, high-resolution USB oscilloscope with a 12-bit vertical resolution, 20 MHz bandwidth, and a maximum sampling rate of 80 MS/s. With a deep memory buffer of 256 MS, it allows detailed signal capture over long durations. The

device includes a 14-bit arbitrary waveform generator and supports advanced signal analysis features such as FFT, serial protocol decoding, and digital triggering, making it suitable for precise and high-fidelity measurements in optical sensing applications. The integrated waveform generator was also used to drive the loudspeaker that simulates the vibrating object, enabling controlled and repeatable excitation during the sensing experiments.

PicoScope 4424A	
Channels	4
Vertical Resolution	12 bits
Bandwidth	20 MHz
Maximum Sampling Rate	80 MS/s
Memory Depth	256 MS
Input Range	±50 mV to ±50 V
Arbitrary Waveform Generator (AWG)	14-bit resolution, 80 MS/s update
Signal Generator Bandwidth	20 MHz (sine)

Figure 3.7 : Specification table of PicoScope 4424A [34].

3.1.5 Fabrication of Tapered Optical Fibers

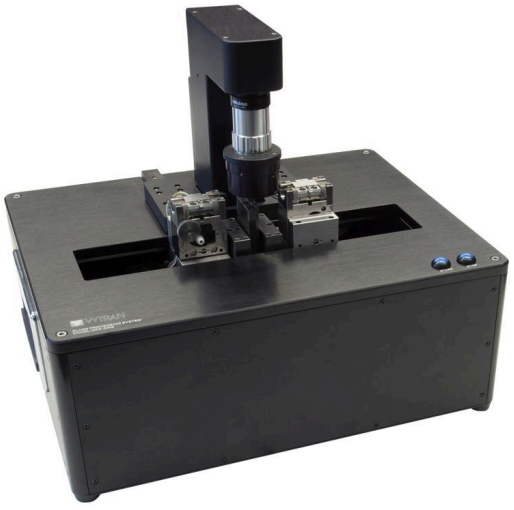

Figure 3.8 : Photography of Vytran® GPX3400.

The Vytran® GPX3400 automated glass processor was employed for the fabrication of the tapered optical fiber structure. The system utilizes a resistive filament heater to locally elevate the temperature of the fiber material above its softening point, while the fiber is subjected to

controlled axial tension. The tapering process is governed via programmable motion of motorized stages, which define the pulling velocities and taper geometry. Fiber alignment was achieved using built-in translational and rotational stages, and real-time imaging was used to monitor the taper formation. The controlled thermal and mechanical environment of the GPX3400 enabled repeatable production of adiabatic taper profiles suitable for optical mode manipulation in our application [33].

3.1.6 Fiber Splicing Process

Figure 3.9 : Photography of Fujikura FSM-45F.

For the connection of the tapered sensing region to the input and output fiber leads—linking the optical source and photodetector—fusion splicing was performed using the Fujikura FSM-45F splicer. The FSM-45F is an arc-based fusion splicer developed for polarization-maintaining and dissimilar optical fibers. It employs a Profile Alignment System (PAS) for core-to-core alignment, along with a motorized θ-alignment mechanism for rotational alignment of the polarization axes. The system supports short cleaved length splicing and utilizes a V-groove driving structure to accommodate a variety of fiber geometries. Splicing parameters are controlled via programmable sweep arc functions, enabling fine thermal tuning during fusion of large-diameter or compositionally mismatched fibers. The splicer also provides real-time power monitoring via a GP-IB interface and incorporates cross-talk estimation for polarization-maintaining fiber evaluation [35].

3.2 Experimental setup and process

In this section, the experimental setup and procedure employed to evaluate the sensitivity of our sensor to vibrations are presented. As previously mentioned, in order to simulate vibrations and micro-vibrations that may occur during the transportation of a fragile object, the use of a vibration generator was deemed necessary. A loudspeaker was selected as the most appropriate choice for generating vibrations, due to its ease of control and its ability to produce a wide range of oscillation amplitudes. The objective of this setup is to detect the vibrations generated by the loudspeaker using the tapered sensing region of the optical fiber.

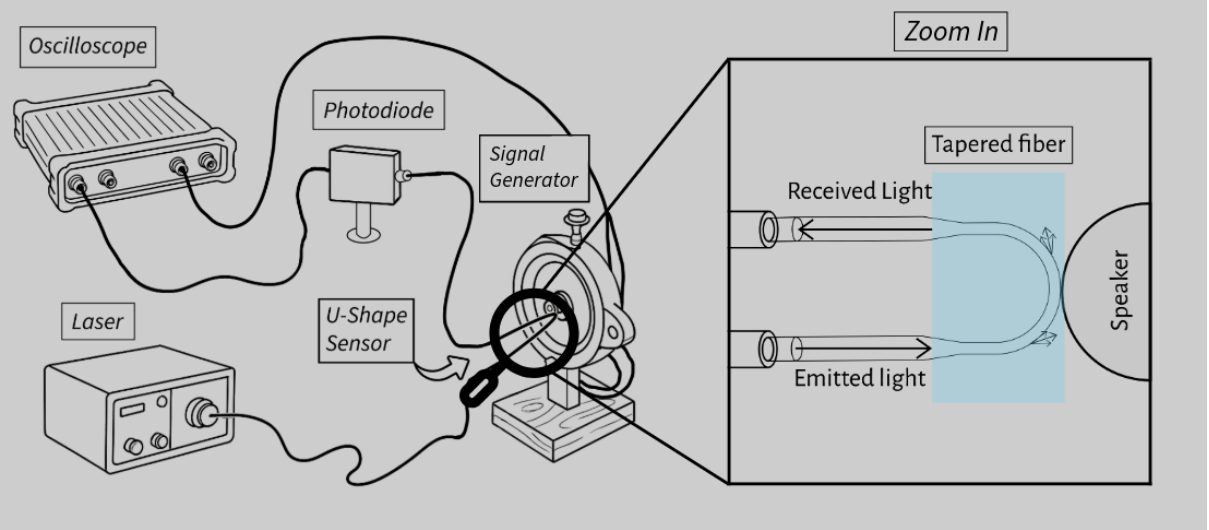

Figure 3.10: Experimental setup.

As illustrated in Fig(3.10), the optical signal originates from the Ando AQ8201-13 Light Source used in our experimental setup and is guided through an SMF-28™ optical fiber. The light has a wavelength of 1550 nm and an output power of approximately 5.5 mW. The fiber is subsequently spliced —using the Fujikura FSM-45F fusion splicer— with the sensing region of our sensor, which is shown in the zoomed-in view of Fig(3.10). This sensing part consists of an SMF-28™ fiber that has been tapered using the Vytran® GPX3400 automated glass processor, a process that increases the fiber's bending losses and, consequently, enhances its sensitivity.

The tapered sensing region is mounted on a micrometric translation stage, which allows for precise positioning with micrometer accuracy. This enables us to align the fiber directly above the loudspeaker. It is important to emphasize that the fiber rests lightly on the loudspeaker without exerting any significant force, making the setup suitable for monitoring vibrations in delicate or fragile systems.

Once the fiber makes contact with the vibrating surface, it begins to follow the oscillatory motion of the speaker, inducing periodic variations in the transmitted optical power as a result of the increased bending losses. The optical signal continues through the SMF-28™ fiber and exits the sensing region, where it is once again spliced to a standard fiber that directs the light toward the measurement instrumentation.

To analyze the optical power variations, the light is converted into an electrical signal using a DET01CFC photodetector. The resulting voltage signal—produced by the photodiode—is transmitted via a 50-ohm BNC cable and monitored using a PicoScope 4424A oscilloscope. It should also be noted, as seen in Fig(3.10), that a second set of cables extends from the oscilloscope to the loudspeaker. These are the driving cables, connected through the Arbitrary Waveform Generator (AWG) functionality of the PicoScope, which allows us to control and modulate the vibration profile of the loudspeaker during the experiment.

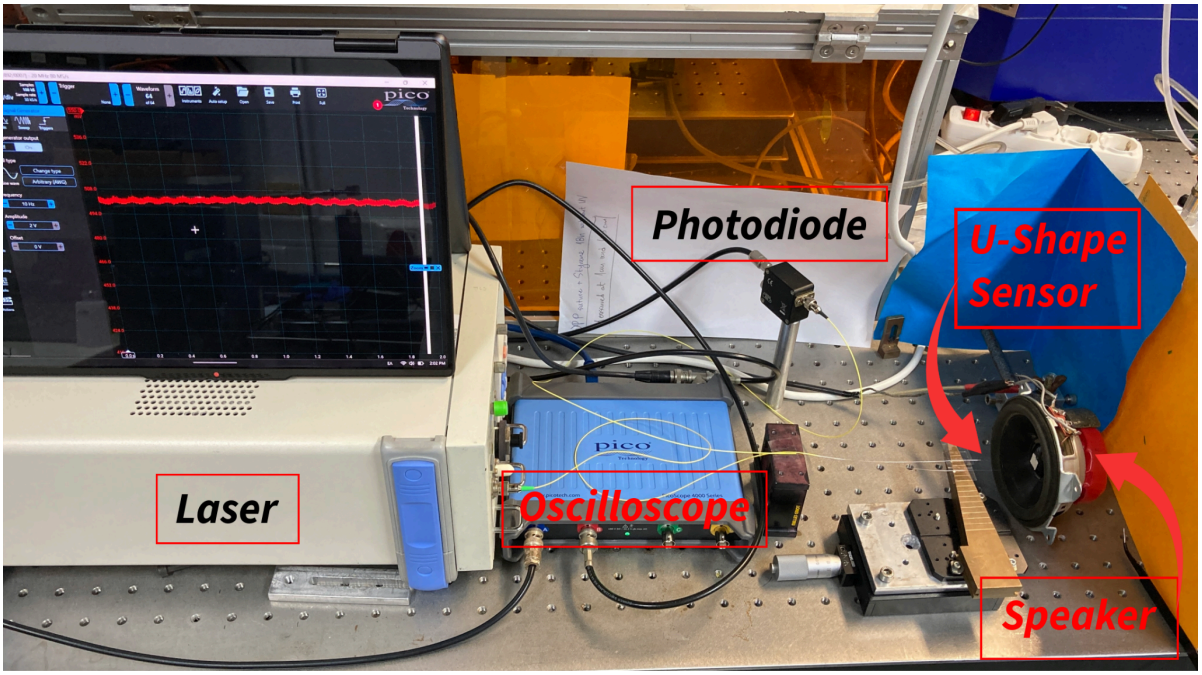

Figure 3.11: Experimental setup photography.

The experiment begins with the generation of various signals using the signal generator. The selection of these signals was made with the aim of evaluating the sensor's ability to detect impacts, vibrations, and different frequency components. To this end, three distinct types of signals were chosen, each designed to test a specific aspect of the sensor’s response.

1. Square signal

The square signal was employed in the experiment to simulate sudden and discrete mechanical impacts. Its sharp transitions between high and low voltage levels effectively mimic abrupt forces or shocks that may occur during the transportation of a sensitive objects. By using this type of signal to drive the loudspeaker, the sensor's ability to detect and respond to rapid, high-intensity vibration events relevant to transport conditions, can be systematically evaluated.

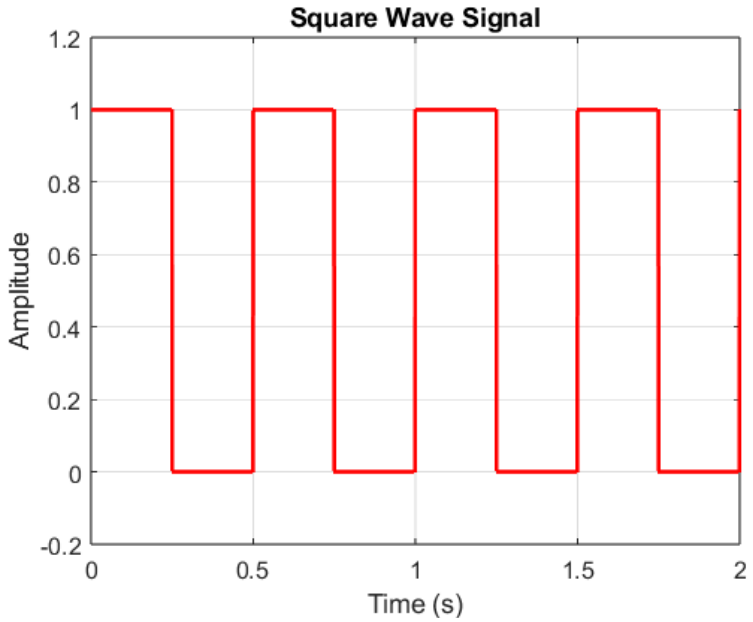

Figure 3.12: Square wave signal at 2 Hz frequency with a duration of 2 second via Matlab.

2. Pseudo-Random Binary Sequence (PRBS) Signal

A Pseudo-Random Binary Sequence (PRBS) is a digitally generated signal that alternates between two discrete levels in a sequence that appears random but is in fact deterministic. It is commonly produced using linear feedback shift registers and is widely used in system identification and communication systems due to its broad spectral characteristics and repeatability. In the context of this experiment, a PRBS signal was used to drive the loudspeaker in order to simulate random, pulse-like mechanical excitations. The use of such a signal enables a more realistic assessment of the sensor’s ability to detect non-periodic and unpredictable vibrations, which are often encountered in practical transport.

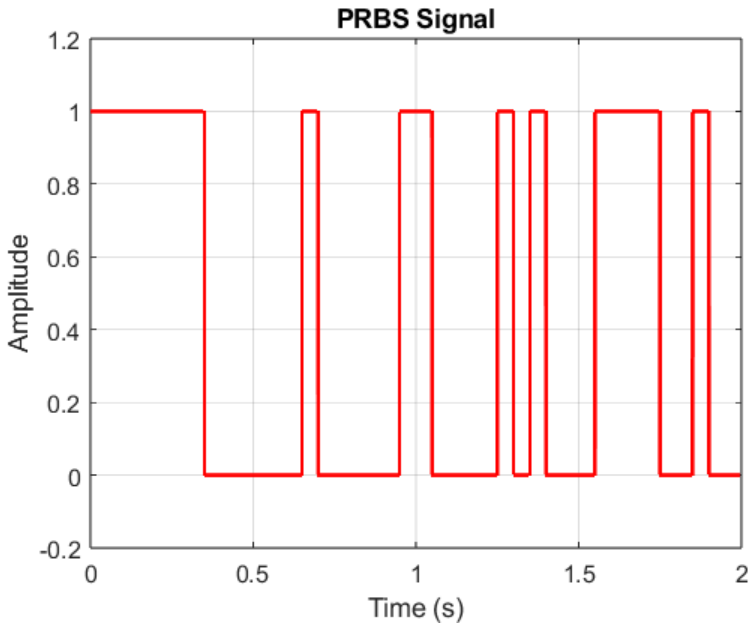

Figure 3.13: PRBS signal at 2 bits/sec over 2 seconds via Matlab.

3. Sinusoidal signal

Sine waves were also used in the experimental process, with the primary objective of evaluating the sensor's ability to detect and respond to vibrations of varying frequencies. In contrast to transient or abrupt excitations, sinusoidal signals provide a stable and continuous waveform that allows for controlled testing across a defined frequency range.

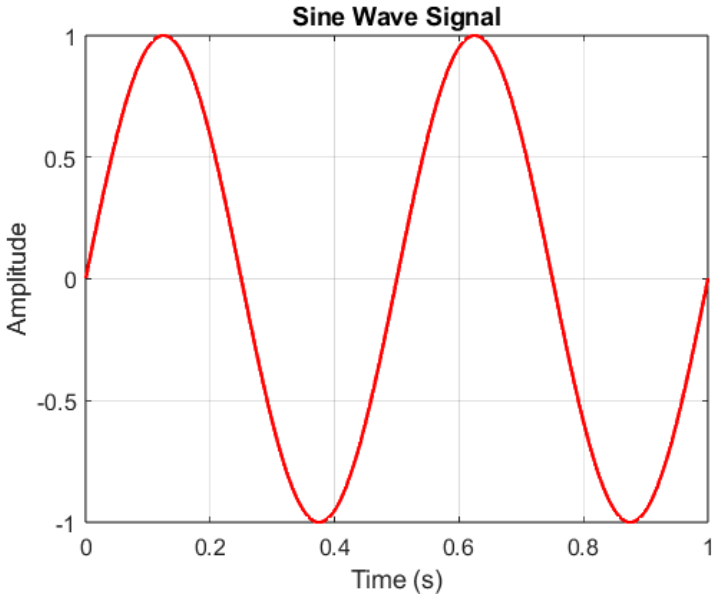

Figure 3.14: Sine wave signal at 2 Hz frequency with duration of 1 second via Matlab.

This approach enables the characterization of the sensor's frequency response and its sensitivity at different spectral components. Furthermore, the use of sinusoidal signals

facilitates the application of Fourier Transform analysis, allowing the extraction of frequency-domain information from the sensor's output.

The Fourier Transform is a mathematical technique that converts a signal from the time —or spatial— domain into the frequency domain. This transformation enables the analysis of a signal's frequency content, allowing the identification of the individual frequency components that constitute a complex waveform. The method is fundamental in various fields such as signal processing, physics, and engineering, as it provides a means for analyzing the spectral composition of time- or space-varying functions [37].

In the context of our experiment, the application of the Fourier Transform allows for the analysis of the sensor's output in the frequency domain, facilitating the evaluation of its response across different frequencies. This is particularly valuable for understanding the sensor's sensitivity to specific spectral components of vibrations that may occur during the transportation of sensitive objects.

As a final experiment, and in order to evaluate all the above simultaneously, it was selected to investigate whether the sensor is capable of perceiving music. If this were achievable, it would imply that the sensor can detect varying frequencies, changes in amplitude, and handle these variations in a non-deterministic sequence.

To this end, a short audio segment was selected that includes pauses, a range of frequencies, and a thematic connection to technology. Specifically, the introductory theme of Super Mario Bros. was chosen. Using MATLAB, the original .mp3 file—shown in Fig. 3.15(a)—was converted into a .wav format to allow its processing through a low-pass filter. This transformation was achieved using the following code :

```
close all;
clear all;
%define the mp3 file
mp3File = 'SuperMarioBros.mp3';
%read the mp3 file
[signal, sampleRate] = audioread(mp3File);
%generate time vector
time = (0:length(rightChannel)-1) / sampleRate;
%plot original signal in time domain
figure;
plot(time, rightChannel);
xlabel('Time (s)');
ylabel('Amplitude');
title('Original Signal');
grid on;
```

```
%apply low-pass filter at 900 Hz
cutoffFreq = 900;
[b, a] = butter(6, cutoffFreq / (sampleRate / 2), 'low');
filteredSignal = filter(b, a, rightChannel);
%plot filtered signal in time domain
figure;
plot(time, filteredSignal);
xlabel('Time (s)');
ylabel('Amplitude');
title('Filtered Signal (Low-pass 900 Hz)');
grid on;
%save the filtered signal as wav
audiowrite('Filtered_SuperMarioBros.wav', filteredSignal, sampleRate);
```

This step aimed to reduce noise and facilitate signal recognition by the sensor. The resulting filtered signal that the sensor was ultimately required to identify is depicted in Fig. 3.15(b).

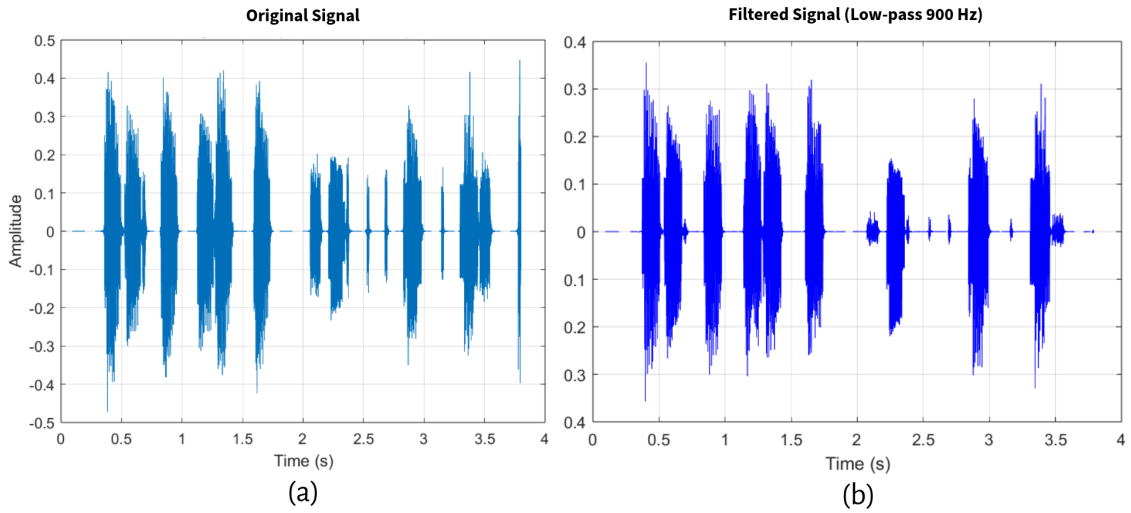

Figure 3.15: Signal of Super Mario Bros and Low pass filtered Super Mario Bros plotted in Matlab.

Subsequently, in order for the .wav file to be compatible with the Arbitrary Waveform Generator (AWG) of the PicoScope, it was necessary to convert it into a comma-separated .csv file. This transformation was achieved using the following code:

```
close all;
clear all;
%read the wav audio file into variable audio and sample rate fs
[audio, fs] = audioread('Filtered_SuperMarioBros.wav');
%set the target number of samples after resampling
targetSamples = 8192;
%get the original number of samples in the audio
originalSamples = length(audio);
%create original sample indices for interpolation
x = linspace(1, originalSamples, originalSamples);
%create new sample indices corresponding to the target samples
xq = linspace(1, originalSamples, targetSamples);
%perform linear interpolation to resample the audio
```

```
resampledAudio = interp1(x, audio, xq, 'linear');
%normalize the audio signal to the range [-1, 1]
resampledAudio = resampledAudio / max(abs(resampledAudio));
%ensure column vector
resampledAudio = resampledAudio(:);
%save the resampled audio data to a comma-separated csv file (PicoScope-friendly)
fid = fopen('SuperMario_AWG_3sec.csv', 'w');
fprintf(fid, '%.6f\n', resampledAudio); % use dot for decimal, no commas
fclose(fid);
```

The signal was successfully uploaded to the AWG module of the PicoScope. Using the PicoScope, the processed Filtered_SuperMarioBros signal was subsequently transmitted in order to drive the speaker. Simultaneously, the sensor's response signal was recorded. In the following chapter, we will examine the degree to which the transmitted and received signals coincide, thereby evaluating the sensor's ability to operate reliably and accurately under these complex conditions.

Figure 3.16: Signal of Low pass filtered Super Mario Bros uploaded to the AWG module of the PicoScope.

Results and Discussion

Chapter 4

In this chapter, the measurements will be presented and discussed. The experiments were designed in such a way that the analysis of the measurements would be straightforward. By having the ability to place side by side the signal that the sensor is expected to detect and the signal that is actually measured, all that needs to be done is to observe whether the two signals match. The signals from the PicoScope channels were collected in .txt format and were directly plotted using MATLAB. For each measurement, at least ten waveforms were recorded in order to verify the repeatability of the experiment. However, due to spatial constraints, only a single representative figure is presented for each case.

However, the PicoScope is not capable of directly monitoring the signal generated by the AWG. Therefore, in order to determine the signal driving the loudspeaker, the voltage across the speaker terminals must be measured. However, this measurement contains not only the source signal but also distortions resulting from the dynamic behavior of the loudspeaker, its impedance, and potentially microphonics — that is, the loudspeaker partially acts as a microphone, capturing ambient sound and converting it into unwanted electrical noise.

To address this issue and to facilitate the comparison between the signal measured by the sensor (Sensor Output) and the signal used to drive the loudspeaker (Excitation Signal), the latter was filtered using MATLAB.

The following command was used:

```
channelB_filtered = movmean(channelB, 5);
```

in order to apply a moving average filter to the excitation signal channelB, with a window size of 5 samples.

In Fig.(4.1), the first measurement using a square signal at 10 Hz is presented. The sensor appears to accurately capture every movement of the loudspeaker, demonstrating its ability to detect abrupt changes as well as bending and stationary states.

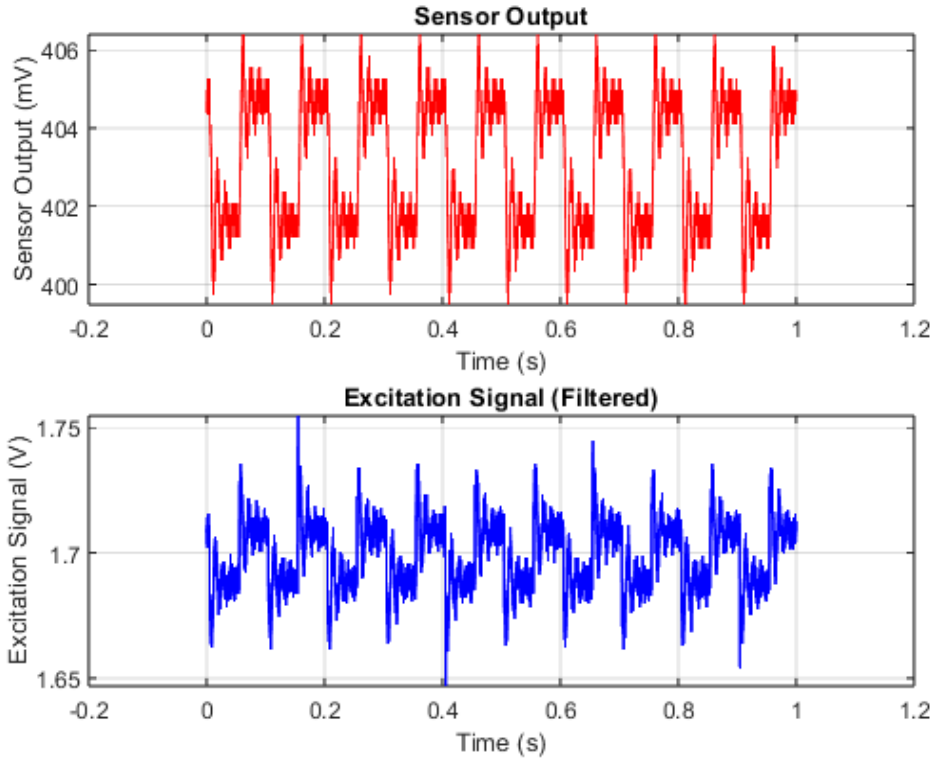

Figure 4.1: Output signal of the sensor and the square excitation signal applied to the loudspeaker at 10 Hz, plotted using MATLAB.

At the peaks and valleys of the signal, some instability can be observed — a form of noise — although the signal would ideally be perfectly flat in these regions. Upon closer inspection, it is evident that this instability does not resemble random white noise, but rather represents a damped oscillation. This is the result of the loudspeaker's inertia: as it reaches its displacement limit with momentum from the previous movement, it momentarily oscillates before settling.

This observation further highlights the sensor's sensitivity and its capacity to detect even the slightest motions of the vibrating object.

Continuing the investigation of the sensor's response to abrupt changes, the element of randomness is introduced in the measurement presented in Fig.(4.2). By using a PRBS (Pseudo-Random Binary Sequence) signal, it is again observed that the sensor accurately follows the motion of the loudspeaker. It is not affected by the random succession of peaks

and valleys, and it demonstrates the ability to remain relatively "noise-free" even during extended low-level regions of the excitation signal.

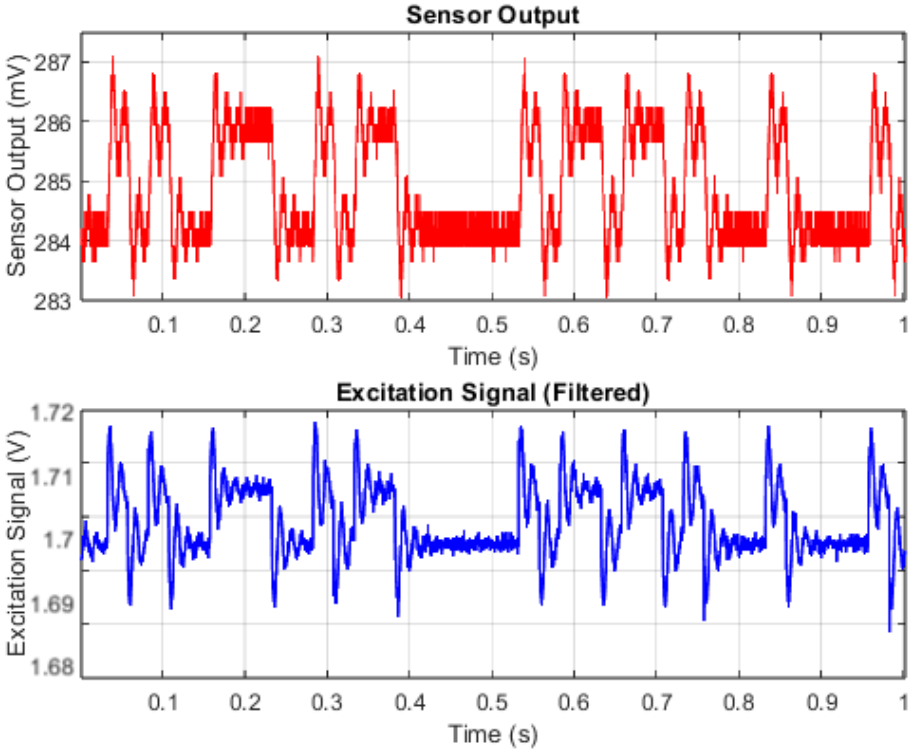

Figure 4.2: Output signal of the sensor and the PRBS excitation signal applied to the loudspeaker at 10 Hz, plotted using MATLAB

As in the previous measurement, damped oscillations are once again observed. However, in this case, the measurement provides further confirmation of the earlier hypothesis. Specifically, in the time intervals from 0.4 to 0.5 seconds and from 0.85 to 0.95 seconds, the signal clearly exhibits a full damped oscillation. As the loudspeaker reaches the valley of the excitation waveform, it has sufficient time to oscillate and settle, thereby confirming the previously discussed interpretation.

In Fig. (4.3), the measurement with the sinusoidal signal at 10 Hz is presented. As in the previous measurements, the sensor signal appears to closely follow the motion of the loudspeaker, accurately capturing the now smooth transitions in its position.

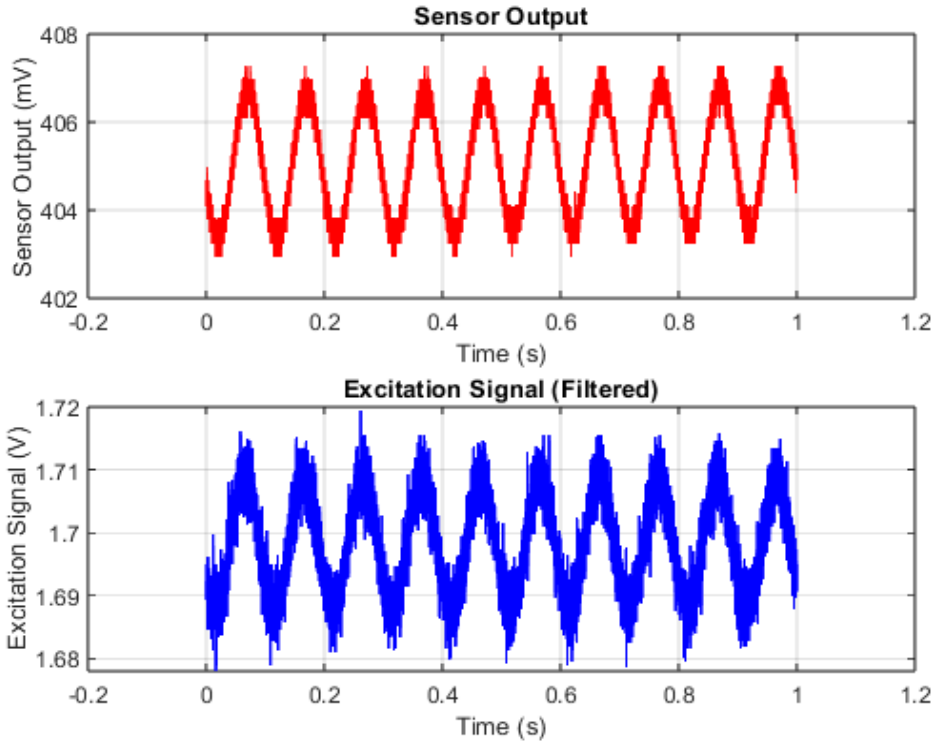

Figure 4.3: Output signal of the sensor and the Sinusoidal excitation signal applied to the loudspeaker at 10 Hz, plotted using MATLAB

At this stage, having acquired all necessary measurements and confirmed the sensor's operational reliability, the next step is to assess its ability to detect different excitation frequencies. To this end, a sinusoidal signal was again used, this time at 40, 140, 240, and 500 Hz, covering a wide frequency range that includes values commonly encountered during the transportation of cargo by truck [38].

Moving into the frequency domain via Fourier Transform, the resulting spectras shown in Figures 4.4 clearly exhibit distinct spikes at the expected frequencies. This demonstrates that, beyond providing clean time-domain signals that can be visually inspected, the sensor also yields data that respond effectively to standard signal analysis methods, confirming its ability to detect and resolve frequency content with clarity and precision.

The following measurements, plotted in MATLAB, present both the theoretical and the measured Fourier Transform (FFT) of the signal. The theoretical FFT was computed based on the expected sinusoidal excitation parameters. A MATLAB marker was placed at the most prominent spectral peak, as visually identified, to highlight the dominant frequency component in each case.

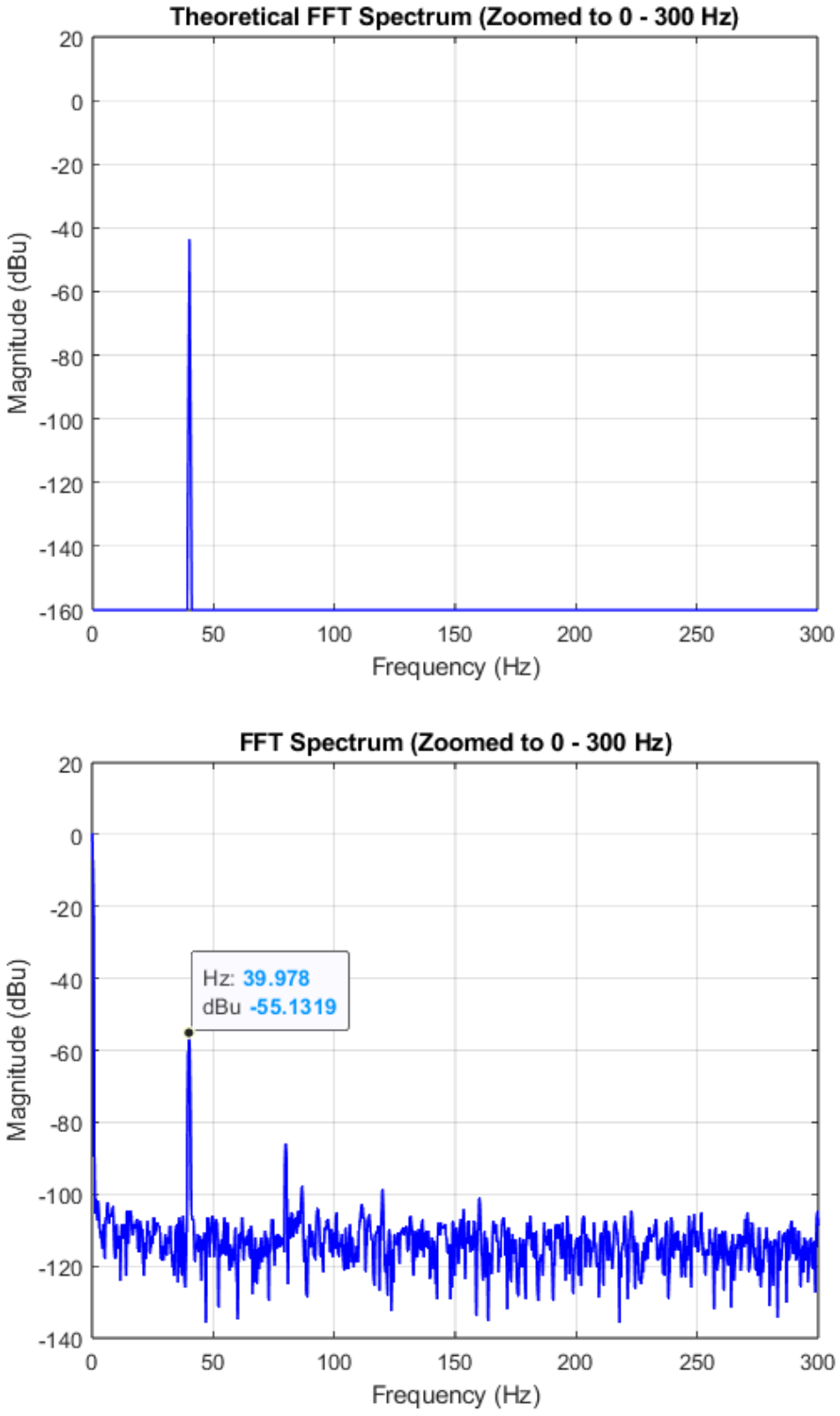

Figure 4.4(a): Theoretical and measured Fourier Transform of the sensor output in response to 40 Hz excitation, plotted using MATLAB.

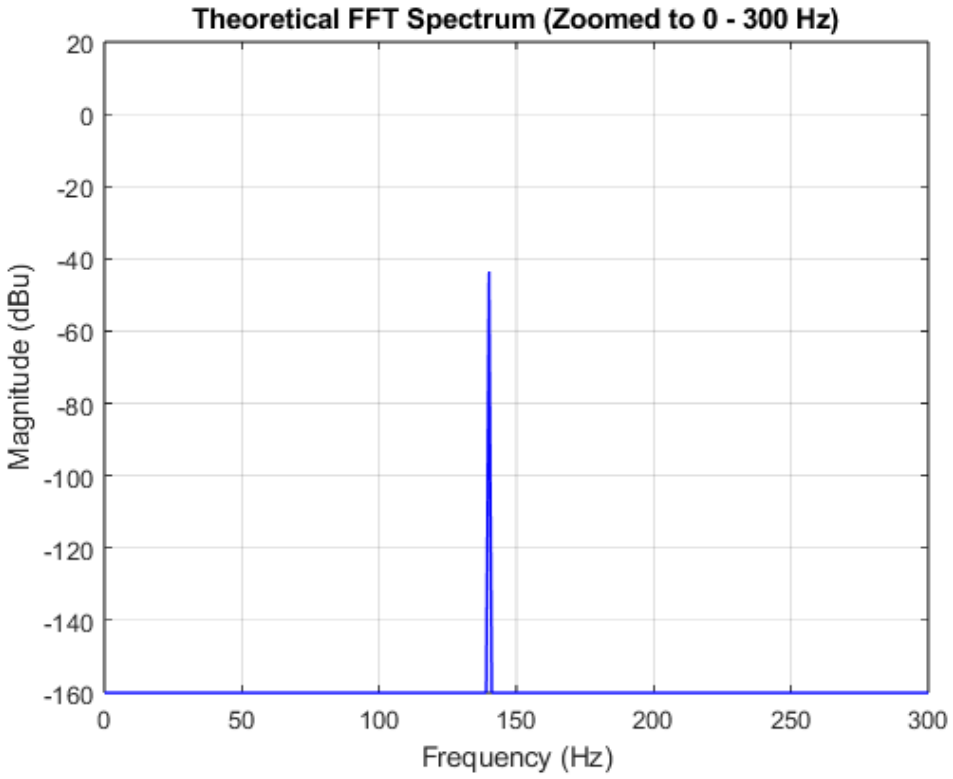

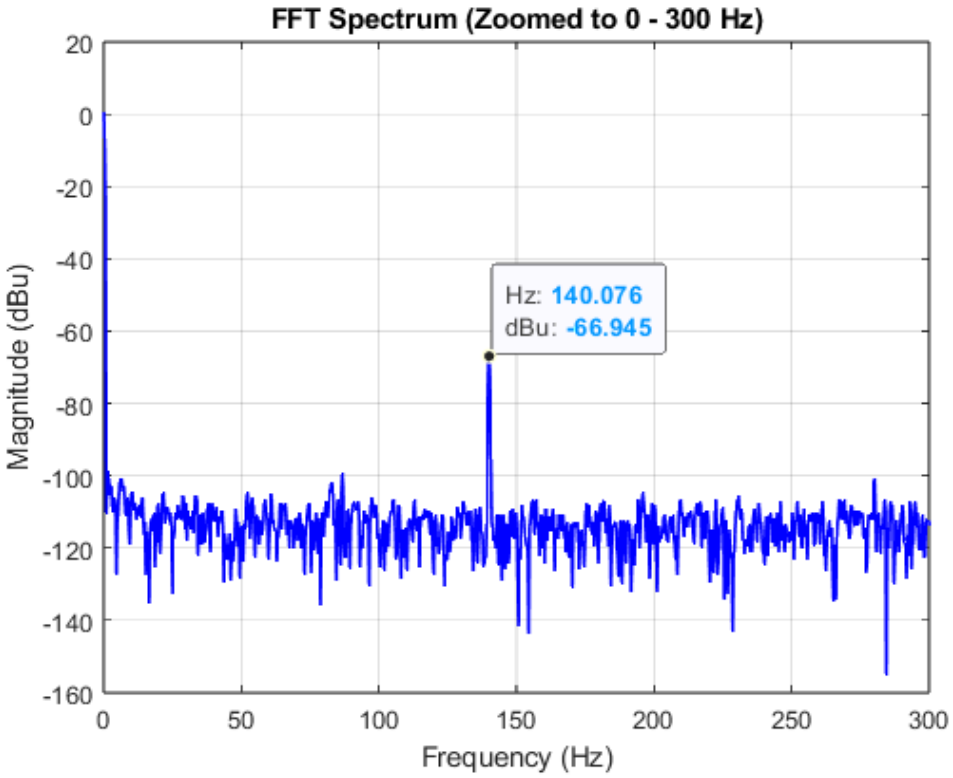

Figure 4.4(b): Theoretical and measured Fourier Transform of the sensor output in response to 140 Hz excitation, plotted using MATLAB.

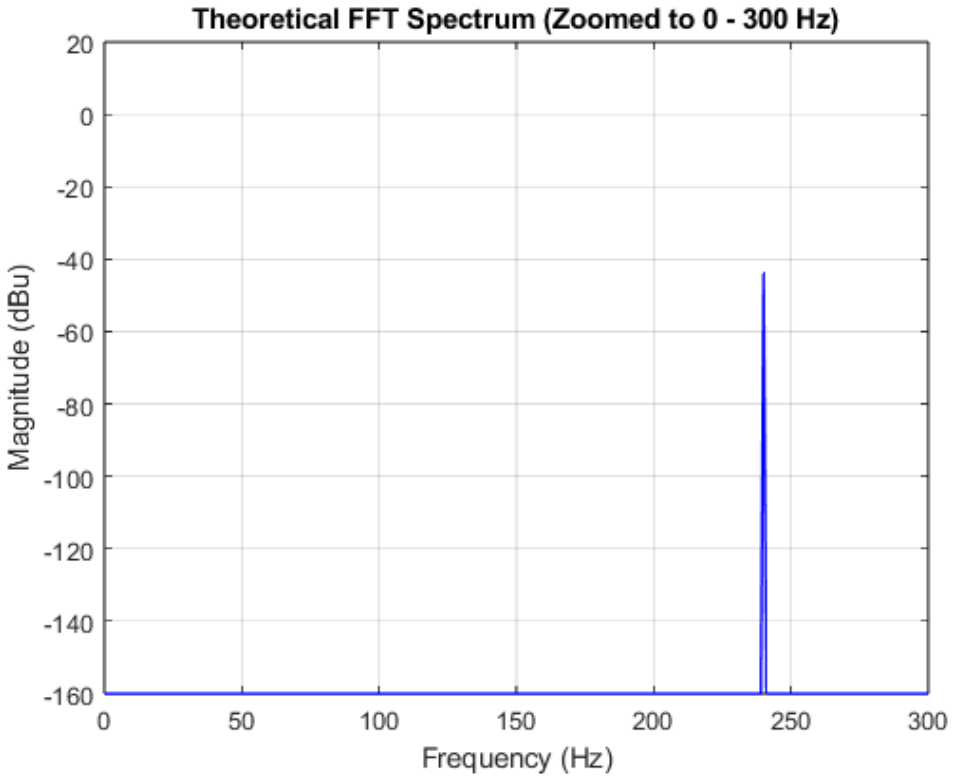

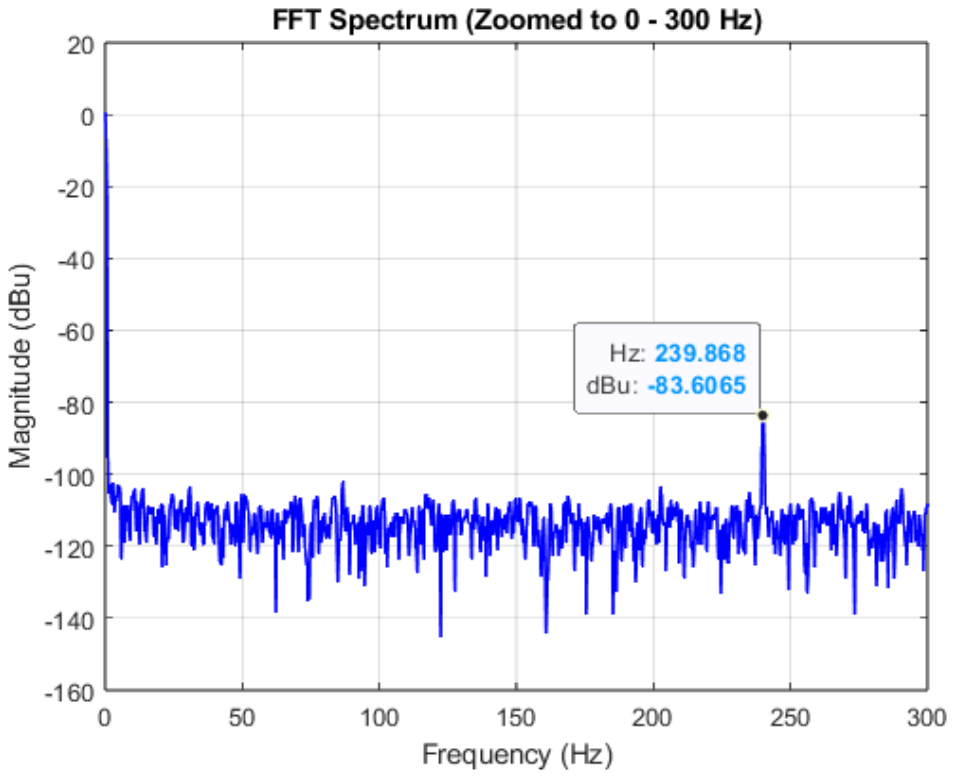

Figure 4.4(c): Theoretical and measured Fourier Transform of the sensor output in response to 240 Hz excitation, plotted using MATLAB.

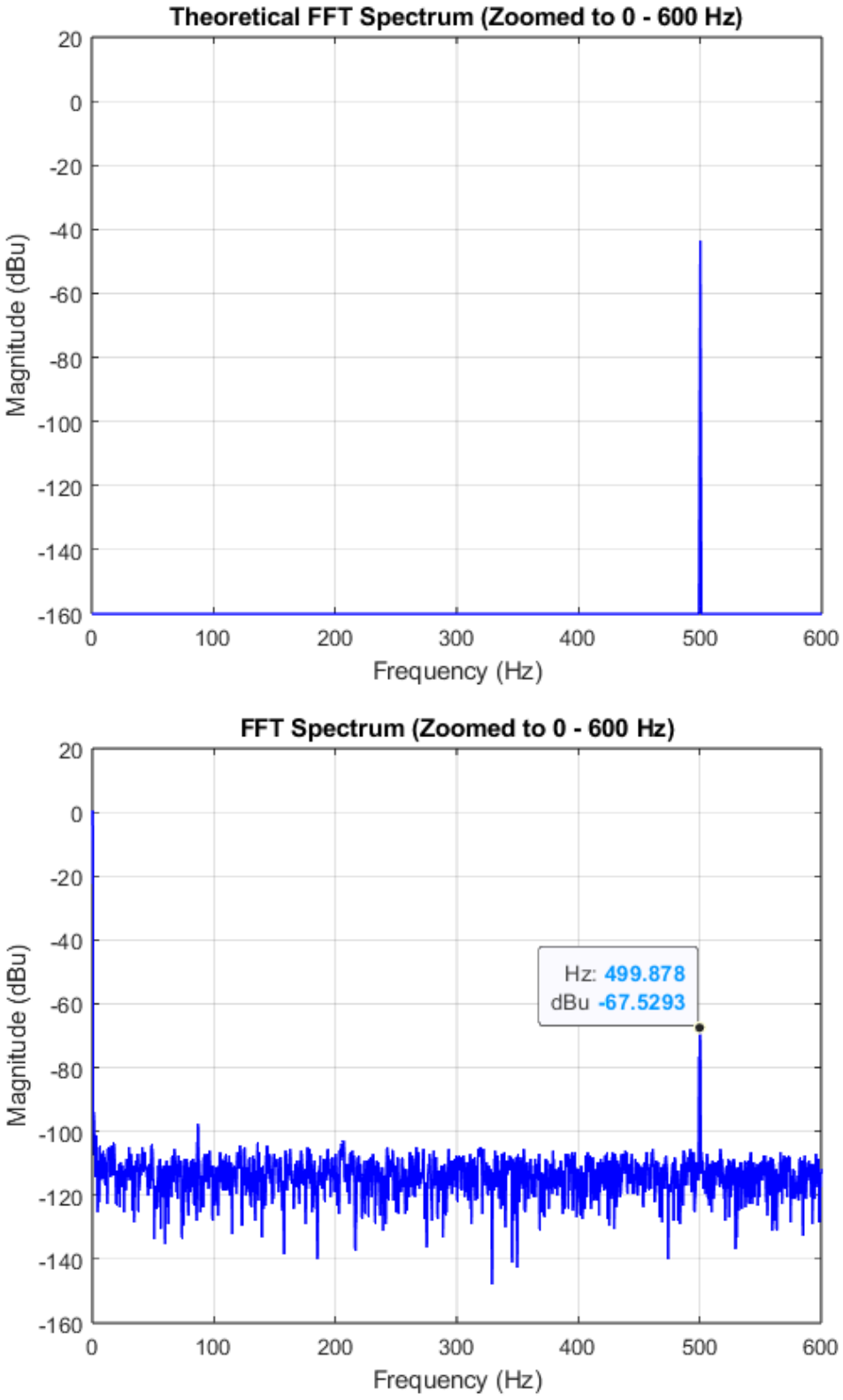

Figure 4.4(d): Theoretical and measured Fourier Transform of the sensor output in response to 500 Hz excitation, plotted using MATLAB.

In Fig. (4.5), the signal detected by the sensor during the measurements, when the Filtered_super MarioBro signal was driving the speaker, is presented. The sensor appears to fully follow the movement of the speaker and accurately capture the song.

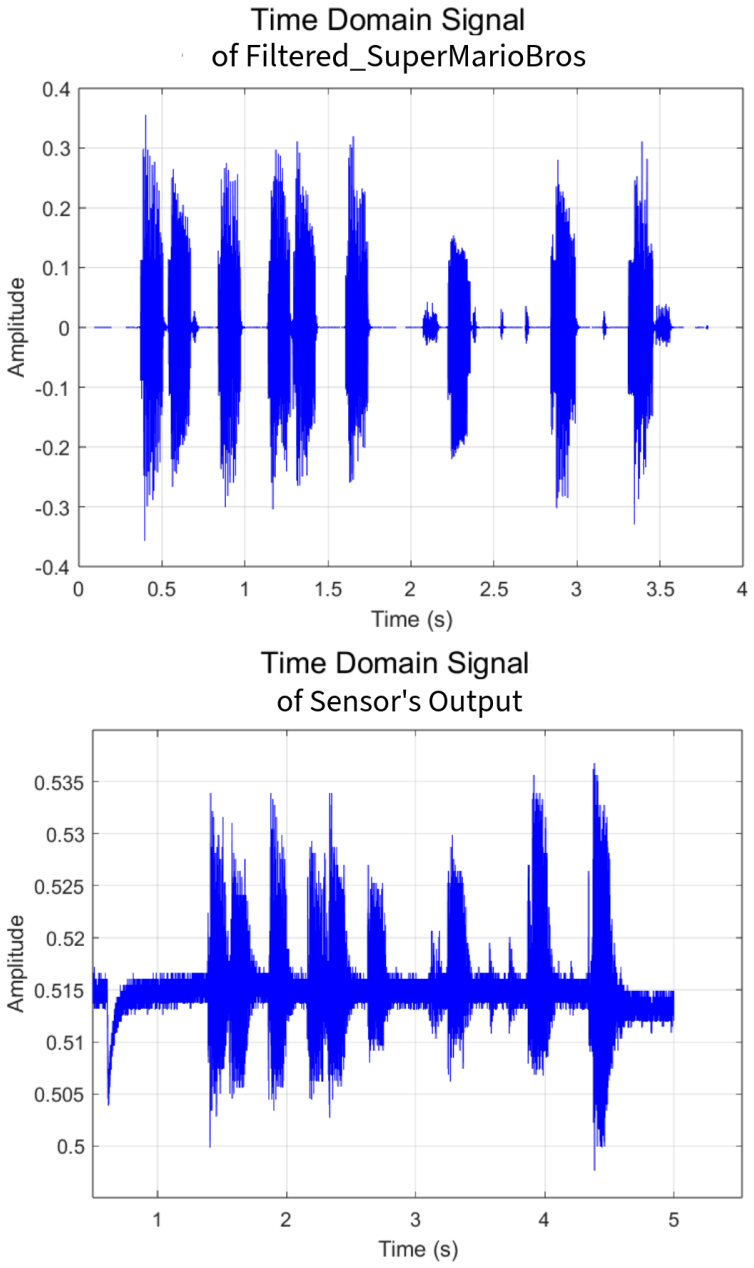

Figure 4.5: Sensor output signal in response to Filtered_SuperMarioBros audio plotted using MATLAB.

However, in order to determine whether the sensor is capable of detecting a signal as complex as a musical piece, an analysis in the frequency domain was required. Therefore, the signals were transformed into the frequency domain using a Fast Fourier Transform (FFT), as shown in Fig. (4.6).

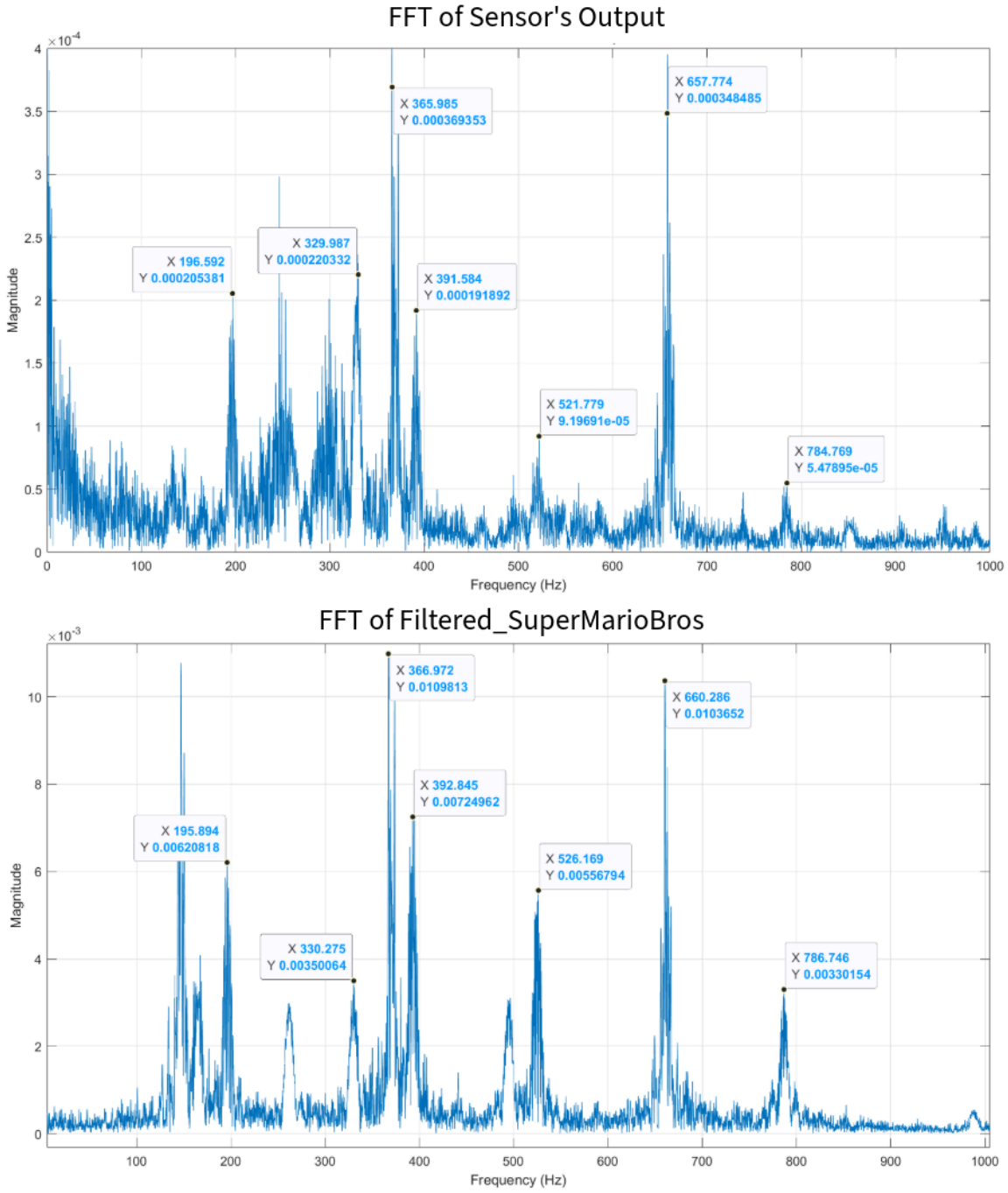

Figure 4.6: Sensor's output signal Fourier Transform compared to Filtered_SuperMarioBros Fourier Transform.

Despite the fact that the measurements were not conducted in a fully soundproof environment, the sensor appears to perceive the main frequencies of the song quite well, even in the presence of noise. Although the amplitude is significantly lower, the fundamental frequencies remain distinguishable, demonstrating the sensor's capability to measure and analyze signals as complex as musical audio.

Conclusion / Future Work

Chapter 5

In this thesis, the development and evaluation of an optical fiber vibrometer for the detection of micro-vibrations in sensitive objects during transportation was presented. The design was based on fundamental principles of light propagation in single-mode optical fibers. A thermally induced tapering process was applied to reduce the fiber diameter, increasing its sensitivity through enhanced bending losses. Upon contact with a vibrating surface, the tapered fiber exhibited measurable changes in transmitted intensity as a result of curvature variations.

The sensor was examined through a series of controlled experiments using both deterministic and stochastic excitation signals, including square waves, pseudo-random binary sequences (PRBS), sinusoids, and processed audio. The recorded responses were analyzed in both time and frequency domains. Frequency-domain analysis, through Fast Fourier Transform (FFT), confirmed the presence of distinct spectral components corresponding to the applied signals. The detection of structured waveforms such as the Super Mario Bros. theme indicated that the sensor was capable of resolving complex vibration patterns under test conditions.

Due to its compact structure and minimal interaction requirements, the sensing scheme can be adapted for use in applications involving fragile objects or artworks. Remote placement of active components such as the light source and photodetector is enabled by the design, allowing for non-contact interrogation through a small segment of fiber in physical contact with the object.

Looking ahead, several exciting directions are foreseen to further enhance the sensor's capabilities and readiness for deployment in critical environments. A key proposal is the coating of the tapered sensing region with a thin, conformal polymer overlay—as discussed in the theoretical section on tapering—to further improve sensitivity by manipulating the

external refractive index. This modification could increase the magnitude of signal response during vibration events.

Another essential step involves the miniaturization of the entire setup for on-site use in heritage preservation. The sensor is planned to be integrated into the conservation efforts at the Foundation for Research and Technology – Hellas (FORTH). In this context, it will be installed directly on works of art to monitor micro-vibrations in real time.

To support this, a compact laser source will be developed based on the SPL1550-5-9-PD DFB laser diode (1550 nm, 5 mW, SM fiber, FC/PC). This diode will be driven by an IC-WK1D PCB-board, a miniature current controller ideal for portable applications due to its compact form factor (6.5 × 20 mm). The conceptual design of this laser source is illustrated in Fig. (5.1).

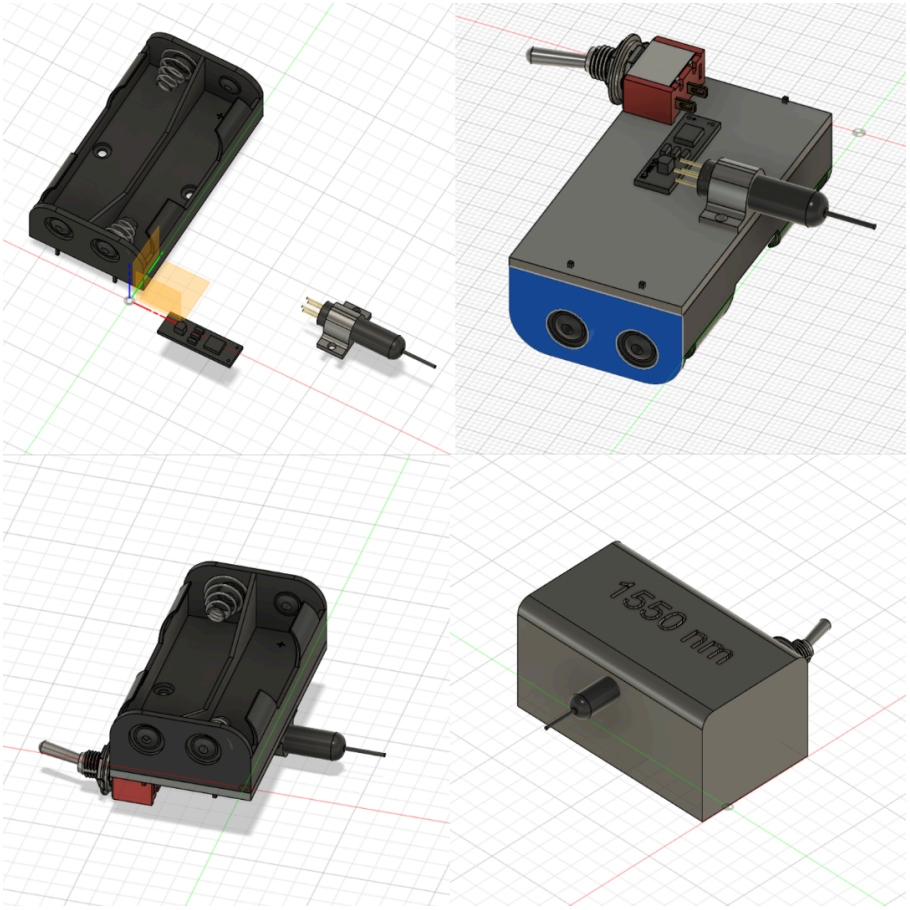

Figure 5.1: 3D Modeling of a Concept Laser Source Designed in Fusion 360 at Actual Scale.

Furthermore, a custom 3D-printed mounting base will be developed to enable precise and reversible installation of the optical fiber onto artworks, ensuring no physical damage. The base will be designed to contact only the wooden stretcher of the painting, thereby avoiding any direct interaction with the canvas and ensuring its preservation, as shown in Fig.(5.2).

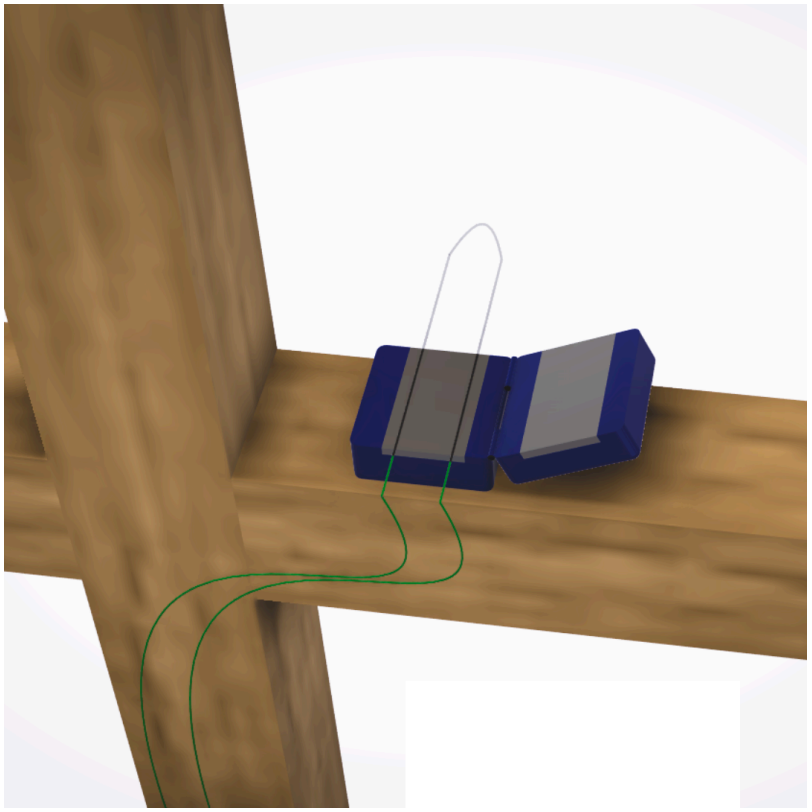

Figure 5.2: 3D Modeling of a Concept mounting base Designed in Fusion 360 at Actual Scale.

In conclusion, the successful lab demonstration of the optical fiber vibrometer lays a robust foundation for practical, real-world deployments. Its adaptability, sensitivity, and modularity hold significant promise for use not only in museum conservation but also in broader domains where mechanical integrity monitoring is paramount.

List of Abbreviations

Abbreviation	Description
OFS	Optical Fiber Sensor
SMF	Single-Mode Fiber
DFB	Distributed Feedback (Laser Diode)
PCB	Printed Circuit Board
AWG	Arbitrary Waveform Generator
PRBS	Pseudo-Random Binary Sequence
FFT	Fast Fourier Transform
ECL	External Cavity Laser
FC/PC	Ferrule Connector / Physical Contact
NIR	Near-Infrared
PAS	Profile Alignment System
GPX	Glass Processing Equipment
LP	Linearly Polarized (mode)
MKS	Meter-Kilogram-Second (unit system)
μm	Micrometer
Hz	Hertz
nm	Nanometer
dB	Decibel
SMA	SubMiniature version A (connector)

References

1. D. L. Lee, *Electromagnetic Principles of Integrated Optics*. New York, NY, USA: Wiley, 1986.
2. I.-L. Bundalo, K. Nielsen, G. Woyessa, and O. Bang, "Polymer optical fiber Bragg gratings for biomedical applications," *Opt. Mater. Express*, vol. 7, pp. 967–979, 2017.
3. M. A. Riza, Y. I. Go, S. W. Harun, and R. R. Maier, "Intelligent photonic sensors for structural health monitoring," *IEEE Sens. J.*, vol. 20, no. 14, pp. 7614–7621, Jul. 2020.
4. S. Yin and P. Ruffin, "Optical fiber sensors," in *Wiley Encyclopedia of Biomedical Engineering*, Hoboken, NJ, USA: Wiley, 2006.
5. L. Liokumovich, A. Medvedev, O. Kotov, S. Markov, and V. Nikolaev, "Fiber optic sensors for environmental monitoring," in *Proc. Linnaeus Eco-Tech*, pp. 527–530, Mar. 2019.
6. G. Kostovski, P. R. Stoddart, and A. Mitchell, "Surface plasmon resonance-based fiber optic sensors," *Adv. Mater.*, vol. 26, no. 21, pp. 3798–3810, 2014.
7. M. I. Zibaii, A. Kazemi, H. Latifi, M. K. Azar, S. M. Hosseini, and M. H. Ghezelaiagh, "SPR sensor based on D-shaped optical fiber," *J. Photochem. Photobiol. B*, vol. 101, pp. 313–320, 2010.
8. B. Xu, J. Huang, L. Ding, and J. Cai, "Electrospun nanofibers for wearable sensors," *Mater. Sci. Eng. C*, vol. 107, p. 110329, 2020.
9. C. Deng, K. Hansen, J. Haus, P. P. Banerjee, and U. Sinha, "Optical fiber sensor for laser-induced diagnostics," in *Proc. SPIE 11238, Optical Fibers and Sensors for Medical Diagnostics and Treatment Applications XX*, San Francisco, CA, USA, 2020.
10. J. Leng and A. Asundi, "Structural health monitoring of smart composite materials by using EFPI and FBG sensors," *Sens. Actuators A Phys.*, vol. 103, no. 3, pp. 330–340, 2003.
11. P. Moyo, J. M. W. Brownjohn, R. Suresh, and S. C. Tjin, "Development of fiber Bragg grating sensors for monitoring civil infrastructure," *Eng. Struct.*, vol. 27, no. 12, pp. 1828–1834, 2005.

12. G. Quattrocchi, P. C. Berri, M. D. L. Dalla Vedova, and P. Maggiore, "Optical fibers applied to aerospace systems prognostics: Design and development of new FBG-based vibration sensors," *IOP Conf. Ser.: Mater. Sci. Eng.*, vol. 1024, no. 1, p. 012095, 2021.
13. T. K. Gangopadhyay, "Prospects for Fibre Bragg gratings and Fabry–Perot interferometers in fibre-optic vibration sensing," *Sens. Actuators A Phys.*, vol. 113, no. 1, pp. 20–38, 2004.
14. G. Perrone and A. Vallan, "A low-cost optical sensor for noncontact vibration measurements," *IEEE Trans. Instrum. Meas.*, vol. 58, no. 5, pp. 1650–1656, 2009.
15. A. M. Abdi and S. E. Watkins, "Strain sensor calibration using extrinsic Fabry–Perot interferometric sensors," *Opt. Eng.*, vol. 46, no. 10, Art. no. 104402, 2007.
16. P. Vaiano et al., "Lab-on-fiber technology: A new vision for chemical sensing," *Laser Photonics Rev.*, vol. 10, pp. 922–961, 2016.
17. A. Palocci, M. Consales, S. Campopiano, A. Cusano, and A. Ricciardi, "Plasmonic fiber-optic biosensors: Recent progress and future prospects," *Adv. Photonics Res.*, vol. 3, p. 2100371, 2022.
18. A. Mendez and T. F. Morse, *Specialty Optical Fibers Handbook*. Amsterdam, The Netherlands: Academic Press, 2007.
19. S. F. Mahmoud, *Electromagnetic Waveguides: Theory and Applications*. Hoboken, NJ, USA: Wiley-Interscience, 1991.
20. E. Hecht, *Optics*, 5th ed. Boston, MA, USA: Pearson Education, 2017.
21. P. Sillard and D. Molin, "A review of few-mode fibers for space-division multiplexed transmissions," in *Proc. 2013 Conf.*, pp. 1–3, 2013.
22. D. Gloge, "Weakly guiding fibers," *Appl. Opt.*, vol. 10, no. 10, pp. 2252–2258, 1971.
23. P. N. Moar et al., "Fabrication, modeling, and direct evanescent field measurement of tapered optical fiber sensors," *J. Appl. Phys.*, vol. 85, pp. 3395–3398, 1999.
24. T. A. Birks and Y. W. Li, "The shape of fiber tapers," *J. Lightwave Technol.*, vol. 10, no. 4, pp. 432–438, 1992.
25. S. W. Harun, K. S. Lim, C. K. Tio, K. Dimyati, and H. Ahmad, "Theoretical analysis and fabrication of tapered fiber," *Optik*, vol. 124, no. 5, pp. 538–543, 2013.
26. Y. Murakami and H. Tsuchiya, "Bending losses of coated single-mode optical fibers," *IEEE J. Quantum Electron.*, vol. QE-14, no. 7, pp. 495–501, Jul. 1978.
27. L. C. Bobb, P. M. Shanker, and H. D. Krumboltz, "Bending effects in biconically tapered single-mode fibers," *J. Lightwave Technol.*, vol. 8, pp. 1084–1090, 1990.

28. P. M. Shankar, L. C. Bobb, and H. D. Krumboltz, "Coupling of modes in bent biconically tapered single-mode fibers," *J. Lightwave Technol.*, vol. 9, pp. 832–837, 1991.
29. J. S. Author(s), "In-line variable optical attenuator based on the bending of the tapered single mode fiber," *J. Opt. Soc. Korea*, vol. 13, no. 3, pp. 349–353, Sep. 2009.
30. L. Jacomme, "Modal dispersion in multimode graded-index fibers," *Appl. Opt.*, vol. 14, no. 11, pp. 2578–2584, 1975.
31. Corning, "Corning SMF-28 Optical Fiber Product Information," [Online]. Available: https://www.health.state.mn.us/communities/environment/risk/docs/guidance/gw/pfoainfo.pdf. [Accessed: Jun. 6, 2025].
32. Artisan Technology Group, "Yokogawa Ando AQ8201-13 ECL Light Source Module – Technical details," [Online]. Available: https://www.artisantg.com/TestMeasurement/54429-41/Yokogawa-Ando-AQ8201-13-ECL-Light-Source-Module. [Accessed: Jun. 6, 2025].
33. Thorlabs, "DET01CFC InGaAs FC/PC-Coupled Photodetector – Specifications," [Online]. Available: https://www.thorlabs.com/thorproduct.cfm?partnumber=DET01CFC. [Accessed: Jun. 6, 2025].
34. Thorlabs, "Vytran Optical Fiber Glass Processors – Documentation," [Online]. Available: https://www.thorlabs.com/newgrouppage9.cfm?objectgroup_id=9326. [Accessed: Jun. 6, 2025].
35. Pico Technology, "PicoScope 4000 Series Oscilloscopes," [Online]. Available: https://www.picotech.com/oscilloscope/4000/picoscope-4000-series. [Accessed: Jun. 6, 2025].
36. Fujikura, "FSM-45F Fusion Splicer – Technical specifications," [Online]. Information retrieved from the product manual. [Accessed: Jun. 6, 2025].
37. G. Karystinos, *Class Notes on Signals and Systems*, TUC, 2022.
38. J. Kim, H. Lee, and C. Park, "Measurement and analysis of vibration levels for truck transport environment in Korea," *Packag. Technol. Sci.*, vol. 20, no. 6, pp. 369–380, 2007.